APRIL 2024 | VOLUME 37

ELSEVIER

APPLIED materialstoday

Cover Caption: Intelligent sensory systems for soft robots predict the natural world

materialstoday
Connecting the materials community

Actions for selected articles

Select all / Deselect all

Download PDFs

Export citations

Show all article previews

Contents

Full-Length Articles

Review Articles

Research article • Full text access

Sodium alginate-polyethylene glycol paste loaded with zinc-doped tricalcium phosphate particles for the treatment of dentin hypersensitivity

Hao Huang, Minjie Fan, Anchun Yang, Dongbiao Chang, ... Jie Weng

Article 102171

View PDF Article preview

Research article • *Open access*

Deposition of high-quality, nanoscale SiO_2 films and 3D structures

Paul Cannon, Enda McGlynn, Darragh O'Neill, Conor Darcy, ... Jennifer Gaughran

Article 102175

View PDF Article preview

Research article • Full text access

Tailoring the heterophase interfacial structures to improve both strength and ductility of Al-Li al by fine tuning major solute Mg

Chengpeng Xue, Junsheng Wang, Xinghai Yang, Xingxing Li, ... Qinghuai Hou

Applied Materials Today 38 (2024) 102171

Contents lists available at ScienceDirect

Applied Materials Today

journal homepage: www.elsevier.com/locate/apmt

Sodium alginate-polyethylene glycol paste loaded with zinc-doped tricalcium phosphate particles for the treatment of dentin hypersensitivity

Hao Huang [a,b], Minjie Fan [c], Anchun Yang [a,b], Dongbiao Chang [a,b], Jinsheng Li [a,b], Liwen Yang [a], Xinlun Li [d], Mengyuan Wang [e], Pengfei Zheng [c,**], Tailin Guo [a,b,*], Jie Weng [a,b,*]

[a] Institute of Biomedical Engineering, College of Medicine, Southwest Jiaotong University, Chengdu, Sichuan 610031, China
[b] Key Laboratory of Advanced Technologies of Materials Ministry of Education, School of Materials Science and Engineering, Southwest Jiaotong University, Chengdu 610031, China
[c] Department of Orthopaedic Surgery, Children's Hospital of Nanjing Medical University, Nanjing 210008, China
[d] Department of Stomatology, Chongzhou People's Hospital, Chongzhou 611230, China
[e] Department of Stomatology, The Third People's Hospital of Chengdu, The Affiliated Hospital of Southwest Jiaotong University, Chengdu, Sichuan 610000, China

ARTICLE INFO

Keywords:
Zn-doped β-tricalcium phosphate
Sodium alginate-polyethylene glycol
Mineralization
Antibacterial
Dentin hypersensitivity

ABSTRACT

β-tricalcium phosphate (β-TCP) has been widely applied in tissue engineering due to its excellent biocompatibility, degradability, and ability to induce mineralization. Zinc ion (Zn^{2+}) displays excellent antibacterial properties and a vital role in regulating cell metabolism. In this context, the incorporation of Zn^{2+} into β-TCP to prepare Zn-doped β-tricalcium phosphate (Zn-β-TCP), emerges as a promising strategy for treating dentin hypersensitivity. However, delivering Zn-β-TCP effectively to the dentin surface for inducing mineralization of dentinal tubules remains a considerable challenge. In this study, we developed a sodium alginate-polyethylene glycol paste loaded with Zn-β-TCP particles, aiming to deliver Zn-β-TCP to the dentin surface for inducing mineralization. Zn-β-TCP particles were synthesized by the hydrothermal method and were combined with a sodium alginate-polyethylene glycol solution to create the Zn-β-TCP/sodium alginate/polyethylene glycol (Zn-β-TCP/SA/PEG) paste. *In vitro* experiments demonstrated that Zn-β-TCP could induce mineralization, exert good biocompatibility and antibacterial activity, promote dentin differentiation of dental pulp stem cells. Furthermore, Zn-β-TCP/SA/PEG exhibited excellent viscosity and effectively prompted the formation of a mineralized layer on dentin surfaces, successfully blocking dentinal tubules. Taken together, the present study demonstrated the potential of the Zn-β-TCP/SA/PEG paste as a promising therapeutic material for the treatment of dentin hypersensitivity.

1. Introduction

Aging and an unhealthy diet can lead to recessionary gums and thinning of tooth enamel, thereby exposing dentin tubules and resulting in dentin hypersensitivity [1]. After the dentin tubules were exposed, external stimuli such as mechanical pressure, temperature changes, chemical agents, and osmotic pressure, etc. could stimulate the nerve endings inside the dentin pulp, resulting in temporary and severe pain or discomfort, which was characterized by dentin hypersensitivity [2]. A survey of seven European countries showed that dentin hypersensitivity affected as much as 41.9% of adults aged 18–35, emphasizing its prevalence as a significant oral health issue [3]. The development of effective biomaterials for treating dentin hypersensitivity has become an urgent problem to be solved in clinical dentistry, and blocking exposed dentin tubules was the key to reducing or curing dentin hypersensitivity [1]. Various substances such as resins, dentin adhesives, and nano-hydroxyapatite (nHA) particles have been widely employed as desensitizing agents for dentin hypersensitivity treatment [4–6]. However, these approaches often yield unsatisfactory clinical outcomes due to their simplistic therapeutic mechanisms that do not fully address the multifaceted requirements of dentin allergy treatment. For instance, nHA particles could induce mineralization on the surface of dentin and thereby block dentin tubules, but they lack antibacterial properties, which meant that they fail to prevent oral bacteria from adhering to the

* Corresponding authors at: Institute of Biomedical Engineering, College of Medicine, Southwest Jiaotong University, Chengdu, Sichuan 610031, China.
** Corresponding author.
E-mail addresses: zhengpengfei@njmu.edu.cn (P. Zheng), tlguo@home.swjtu.edu.cn (T. Guo), jweng@swjtu.edu.cn (J. Weng).

https://doi.org/10.1016/j.apmt.2024.102171
Received 28 November 2023; Received in revised form 8 March 2024; Accepted 20 March 2024
Available online 27 March 2024

mineralized layer wrapped by the salivary fluid-acquired membrane (SAP) to form biofilms that could lead to pulpitis [7]. Moreover, achieving effective drug delivery to the dentin surface while maintaining proper adhesion timing was critical for the successful treatment of dentin hypersensitivity. However, drug delivery platforms designed for application on the tooth surface with good adhesion to prevent/treat allergic reactions have not been fully studied [8]. The ideal drug delivery material for the treatment of dentin hypersensitivity should have good biocompatibility, underwater adhesion, mineralization-inducing capabilities, mechanical compatibility, antibacterial activity, and degradability.

β-tricalcium phosphate (β-TCP) was widely used as a drug carrier and bone defect repair material, owing to its good biocompatibility, bone-inducing and conducting properties, and rapid degradation rate [9–11]. Related studies have shown that β-TCP has an excellent ability to induce mineralization and inhibit tumor recurrence *in vitro* [12,13]. In addition, β-TCP nanoparticles also enhanced the micro-tensile bonding strength of experimental adhesives and produced appropriate dentin interactions [14]. In recent years, zinc (Zn) has been called the "calcium of the 21st century", and Zn-based biodegradable biomaterials have become emerging biomaterials due to their inherent physiological correlation, biocompatibility, biodegradation, and regenerative properties [15]. Notably, Zn^{2+} contributed not only to regeneration and metabolism but also exhibited notable bacteriostatic effects [16,17]. Zn^{2+} released from Zn-based ceramic materials may interact with bacterial surfaces, alter charge balance and prompt cell deformation and lysozyme [18]. Zn^{2+} could modulate the physical and chemical properties of bioceramics, thereby improving their biological functions. Moreover, Zn^{2+} released from bioceramics could significantly promote the proliferation and differentiation of rat and human bone marrow cells [19,20]. Sodium alginate (SA), a naturally derived polysaccharide isolated from the cell wall of brown algae, has been approved by the Food and Drug Administration (FDA) for commercially available hydrogel dressings, such as Purilon Gel (Coloplast Ltd.), Nu-Gel Hydrogel (Systagenix Wound Management Ltd.) and Flaminal Hydro Alginate Gel (Flen Health UK Ltd.) [21]. SA was biodegradable under physiological conditions and readily formed gels through divalent cation chelation, thereby promoting mineralization [22,23]. Given its non-toxic, non-immunogenic nature, favorable biocompatibility, and resistance to protein adsorption, polyethylene glycol (PEG) has found extensive application in biomedical drug delivery, tissue engineering, and surface modification [24,25]. The carboxyl group of PEG could chelate with calcium ions and induce the mineralization of calcium phosphate, so it was suitable for bone repair material [26,27]. The viscosity of PEG aqueous solution increased with molecular weight augmentation, while low molecular weight PEG was relatively toxic [28,29]. In addition, PEG served as an effective carrier to enhance drug and protein loading efficacy and delivery outcome, while concurrently inhibiting bacterial adhesion to reduce the formation of biofilm [30,31]. Chen et al. confirmed that the oligomer formed by amyloid aggregation of lysozyme coupled with PEG could induce *in-situ* remineralization in dentin tubules for dentin hypersensitivity treatment [32]. PEG and SA were polycations and polyanions respectively, and they could form polyelectrolyte complexes to improve the effect of mineralization and the repair of bone tissue [33]. Given the oral environment's humid nature and the friction exerted by daily dietary consumption on dentin surfaces, therapeutic materials should contain good viscosity in the underwater environment to avoid drug shedding. Patil et al. have confirmed that the aqueous solution of PEG-4000 possessed good viscosity [34].

In this study, a paste prepared by the mixture of sodium alginate, PEG-4000, and Zn-β-TCP showed a good mineralization-inducing effect, antibacterial effect, and reliable adhesion, which could serve as an effective carrier for delivering Zn-β-TCP to the dentin surface, effectively prompting mineralization processes. Consequently, dentinal tubules were blocked to achieve the effect of treating dentin hypersensitivity, as shown in Fig. 1.

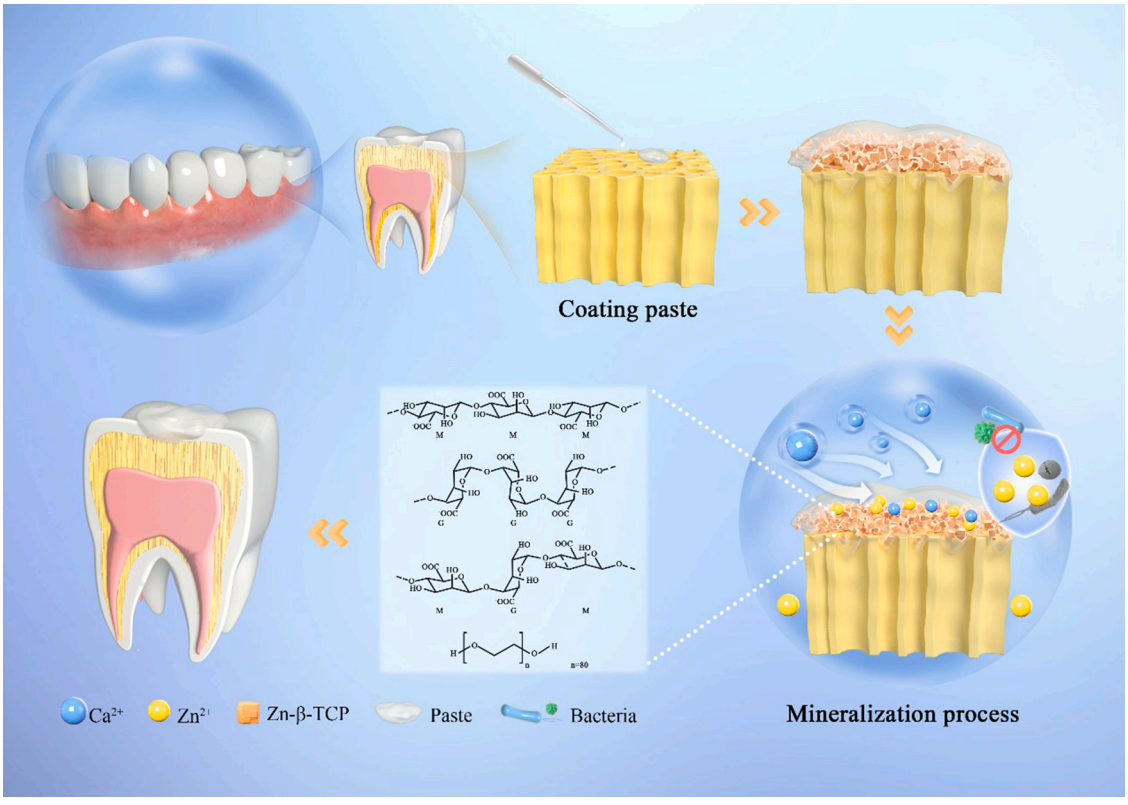

Fig. 1. Schematic diagram of Zn-β-TCP/SA/PEG paste with antibacterial and mineralization-inducing properties for the treatment of dentin hypersensitivity.

2. Materials and methods

2.1. Materials

Calcium nitrate tetrahydrate [$Ca(NO_3)_2{\cdot}4H_2O$, AR], zinc nitrate hexahydrate [$Zn(NO_3)_2{\cdot}6H_2O$, AR], diammonium hydrogen phosphate [$(NH_4)_2HPO_4$, AR] were purchased from Chengdu Kelong Chemical Reagent Factory, and ammonium hydroxide (AR) was sourced from Chuandong Chemical Co., Ltd (Chongqing, China). Sodium alginate (AR) and Polyethylene glycol-4000 (PEG-4000) were purchased from Aladdin (Shanghai, China). β-TCP particles (Size: 0.5–5.0 μm) were provided by Nanjing Junzhuo Chemical Co., Ltd. The simulated body fluids (SBF) were provided by Coolaber (Beijing, China), and phosphate-buffered saline (PBS) was sourced from Servicebio (Wuhan, China). Relevant reagents for cells including dulbecco's modified eagle (DMEM) medium, fetal bovine serum, penicillin-streptomycin solution, and DMEM high glucose medium were provided by ThermoFisher (Hyclone, America) with trypsin were purchased from Labgic (Biosharp, Beijing, China). Calcein/Propidium iodide (PI) cell viability/cytotoxicity assay kit and Cell Counting Kit-8 (CCK-8) was purchased from Beyotime (Shanghai, China). RNAiso Plus (9109) was provided by Takara (Beijing, China). Trichloromethane (AR), isopropanol (AR), and anhydrous ethanol (AR) were purchased from Sinopharm Chemical Reagent Co. Ltd. (Shanghai, China). RT OR-EasyTM II (220,303) was provided by Foregene (Chengdu, China). SYBR®Green Realtime PCR Master Mix and primers were procured from Genesand (SQ412, Beijing, China) and Tsingke (Beijing, China), respectively. Blood agar medium was provided by BKMAM (Changde, China). The CO_2 production bag (C3) and incubation bag (C41) were provided by Mitsubishi Chemical Corporation (Japan). Brain heart infusion (BHI) broth and simulated saliva were purchased from Solarbio (Beijing, China). All reagents were used without further purification unless mentioned especially.

2.2. Synthesis of Monetite, S-Zn-β-TCP, and B-Zn-β-TCP

A certain amount of $Ca(NO_3)_2{\cdot}4H_2O$ and $Zn(NO_3)_2{\cdot}6H_2O$ were added to a beaker containing 50 mL of deionized water, ensuring that the concentration of (Zn^{2+}+Ca^{2+}) was 2.0 M, Zn^{2+}/(Ca^{2+}+Zn^{2+})= 0.1 (molar ratio), and stirred until complete dissolution to form solution A. A quantity of $(NH_4)_2HPO_4$ was dissolved in a beaker containing 50 mL of deionized water, ensuring that the concentration of P was 1.2 M, and stirred until complete dissolution to form solution B. Solution B was added dropwise to solution A at a rate of 8 mL/min to form a white emulsion under stirring state. Continue stirring for 5 min after the dripping process was over, then 2 mL of ammonia hydroxide was added, and continue stirring for 20 min. Subsequently, 40 mL of the resulting emulsion was removed, and 325 μL of ammonium hydroxide was added to it. The mixture was stirred for 5 min, and then the obtained white emulsion was transferred to a reaction kettle for further reaction to obtain a small size of Zn-β-TCP particles [denoted as S-Zn-β-TCP]. Next, solution B was slowly added dropwise to solution A at a rate of 8 mL/min under a stirring state, resulting in a white emulsion. Continue stirring for 5 min after the dripping process was over, and then 1.5 mL of ammonium hydroxide was added, and stirring continued for 25 min. The resulting emulsion was then transferred to a reaction kettle for further reaction to obtain a big size of Zn-β-TCP particles [denoted as B-Zn-β-TCP]. The preparation procedures for the Monetite were the same as those of B-Zn-β-TCP, except that $Zn(NO_3)_2{\cdot}6H_2O$ was not added. The reaction condition was 150 °C and 8 h.

2.3. Fabrication of SA/PEG-4000, Monetite/SA/PEG-4000, and S-Zn-β-TCP/SA/PEG-4000 paste

To prepare the paste of S-Zn-β-TCP/SA/PEG-4000, 4.0 g of S-Zn-β-TCP were dispersed in a 50 mL beaker containing 20 mL of deionized water, and stirred until the uniform emulsion was formed. The resulting emulsion was then placed in a water bath with stirring and heating, and 0.2 g of sodium alginate was added to the emulsion and stirred when the temperature was up to 60 °C. After the sodium alginate was completely dissolved, 0.4 g of PEG-4000 was added to the mixture and stirred while heating for 2 h until the white paste was formed. The same procedures were followed to prepare the B-Zn-β-TCP/SA/PEG-4000 paste and Monetite/SA/PEG-4000 paste. Except for not adding PEG-4000, the preparation processes of Monetite/SA and S-Zn-β-TCP/SA were the same as the Monetite/SA/PEG-4000 and S-Zn-β-TCP/SA/PEG-4000, respectively.

2.4. Preparation of tooth slices

The human third molars were collected from the Third People's Hospital of Chengdu, and the collected teeth were immersed in 75% ethanol solution and then dried at 37 °C for 48 h after the soft tissue was removed. The tooth slices were cut with a hard tissue slicer (SP1600, Leica, Germany) to a size of 5 mm in length, 5 mm in width, and 1 mm in thickness, as illustrated in Fig. 8(A). Subsequently, the slices were polished with 800# and 1200# sandpaper, with the polished surface being the side near the crown. The tooth slices were decalcified by immersing them in EDTA solution at pH= 8.0 for 40 min and then sonicated in the EDTA solution for 10 min after the polishing process was over. The slices were then washed twice with deionized water after the decalcification was complete and then stored in 0.1% thymol solution for future use.

2.5. The characterization of samples

The morphology and elemental distribution of samples were investigated by a scanning electron microscope (SEM, JSM7800F) equipped with the energy dispersive X-ray spectrometer (EDS), while the physical phase and chemical structure of samples were examined by X-ray diffractometer (XRD, Philips PW3040/60, Cu-Kα, 35 mA, 45 kV) and Fourier transform infrared spectrometer (FTIR, 500–3500cm^{-1}, Thermo Nicolet 5700). Furthermore, the element content in the samples and the amount of zinc and calcium released during the mineralization process were determined by inductively coupled plasma atomic emission spectrometry (ICP-AES, Spectro Arcos, Speicher Germany).

2.6. The mineralization of Monetite, S-Zn-β-TCP, and B-Zn-β-TCP in vitro

0.4 g of Monetite, β-TCP, S-Zn-β-TCP, and B-Zn-β-TCP were added to the centrifuge tube containing 40 mL of artificial saliva, respectively. The tubes were then placed in a shaker (100 rpm, 37 °C) for 1, 4, and 7 days. At the corresponding time points, the mineralization process was terminated by washing the samples three times with acetone followed by washing twice with deionized water after the supernatants were collected. The samples were then collected and subjected to relevant characterization. The mineralization in simulated body fluid was performed as the same procedure described above.

2.7. Evaluation of viscosity of the paste

To test the viscosity of the paste, 20 μL of Zn-β-TCP/SA and Zn-β-TCP/SA/PEG-4000 were coated on the surface of tooth grooves, respectively. Then the tooth grooves before and after scouring (40 mL/min, 15 mL) were photographed and recorded, and the viscosity of Zn-β-TCP/SA and Zn-β-TCP/SA/PEG-4000 was evaluated by comparing the residual paste on the surface of the tooth grooves.

2.8. Preparation of extract solution

0.4 g of the Monetite, S-Zn-β-TCP, and B-Zn-β-TCP was added to centrifuge tubes containing 40 mL of PBS, respectively. The centrifuge tubes were then placed in a shaker (100 rpm, 37 °C) and shaken for 7

days. After the release period, the supernatant was collected by centrifugation and subsequently filtered through the membrane filter to remove bacteria present for further use.

2.0 g of sterilized Monetite, S-Zn-β-TCP, and B-Zn-β-TCP (high-pressure steam sterilization, 120 °C, 2 h) were added to centrifuge tubes with 40 mL of DMEM with high sugar (or α-MEM) and then the centrifuge tubes were placed in a shaker (100 rpm, 37 °C) for 7 days. The mixtures were centrifuged (6000 rpm, 3 min) to collect the supernatants when the release process was finished. After the supernatants were filtered through the membrane filter to remove bacteria, 10% FBS and 1% penicillin/streptomycin were added to the above-mentioned supernatants to form an ion extract-contained α-MEM culture medium, and then the solution was well shaken and placed in a refrigerator at 4 °C for storage.

2.9. Sources of bacteria and cells

The Streptococcus mutans (ATCC25175) was procured from Taisituo (Ningbo, China). Rat primary dental pulp stem cells (RAT-iCell-m012, DPSCs) were obtained from iCell Bioscience Inc (Shanghai, China). Bone marrow mesenchymal stem cells (BMSCs) were isolated from the femurs of SD rats (1-month-old, male), which were purchased from Dashuo Biotechnology (Chengdu, China).

2.10. Evaluation of antibacterial ability in vitro

50 μL of Streptococcus mutans solution with a bacterial concentration of 4×10^8 CFU/mL was mixed with 450 μL of extract solution in a 24-well plate. The mixture was put into an incubation bag and incubated in a bacterial incubator (37 °C) for 12 h and 24 h, respectively. 50 μL of bacterial solution was mixed with 450 uL of sterile PBS set as the control group. After incubation, 100 μL of the mixture was transferred into a 96-well plate and the absorbance value (wavelength= 450 nm) was measured by a microplate reader. Three parallel samples were set up for each group, and the experiment was repeated three times.

20 μL of Streptococcus mutans solution with a bacterial concentration of 4×10^8 CFU/mL and 200 μL of extract solution were uniformly coated on a blood plate, sealed, and incubated in a CO_2 gas-producing bag in the bacterial incubator (37 °C) for 24 h. 20 μL of bacterial solution and 200 μL of sterile PBS co-coated plate set as the control group. After incubation was finished, the growth of bacterial colonies was observed and photographed. Three parallel samples were set up for each group, and the experiment was repeated three times.

2.11. Evaluation of biocompatibility in vitro

DPSCs were prepared as cell suspension and were seeded in the 48-well plate at a density of 1×10^4 per well (2×10^4/mL), the plate was put into a cell incubator (37 °C, 5% CO_2) and cultured overnight until the cells adhered. Subsequently, the medium was substituted with 500 μL of extract solution from the Monetite, S-Zn-β-TCP, and B-Zn-β-TCP, while DMEM with high sugar containing 1% amphotericin B/streptomycin/penicillin solution and 15% FBS was set as the control group. The culture medium was replaced every two days, and the CCK-8 assay was performed to detect cell viability on days 1, 3, and 5. On the fifth day, the DPSCs were rinsed with PBS three times after the medium was removed. Subsequently, 200 μL of live/dead staining working solution was added to each well and incubated for 15 min at 37 °C according to the manufacturer's instructions. After incubating, the staining was observed and recorded by a fluorescence microscope.

BMSCs were seeded in 24-well plates with a density of 6×10^3 cells per well with the addition of 0.5 mL of medium, followed by incubation in the cell culture incubator for 2 days, and the medium was replaced once a day until the cells adhered to the wall. Subsequently, the original medium was removed and 1.0 mL of extract solution was added to each well, and incubated for 1, 3, and 5 days with the medium changed every two days, and α-MEM served as the control group. On days 1, 3, and 5, the cell viability of BMSCs was detected by the CCK-8 assay. On day 5, cells were washed with PBS three times and double-stained with calcein-AM (Biotum, USA) and propidium iodide (Biotum, USA) according to the manufacturer's instructions. The fluorescent images of cells were captured by an inverted fluorescence microscope (Nikpc Ti-U, Nikon, Japan) equipped with a digital camera (40FL Axioskop, Zeiss, Germany).

2.12. Evaluation of dentinogenic differentiation in vitro

To examine the expression of dentinogenic-related genes of DPSCs, a real-time quantitative polymerase chain reaction (qRT-PCR) was performed. The DPSC were seeded in 48-well plates with a density of 6×10^3 cells per well with 300 μL of medium and incubated overnight for cell attachment. Subsequently, the original medium was replaced with the extract medium, and the medium was changed every two days. At the end of the culture, the DPSCs were washed twice with PBS, and 1.0 mL of Trizol was added. The cells were gently scraped off from the culture plate and left at room temperature for 5–10 min to allow complete lysis. After that, the lysate was transferred into 1.5 mL RNase-free centrifuge tubes to proceed with the RNA extraction. 200 μL of chloroform was added after the transfer process was finished, and the mixture was shaken and mixed for 30 s. The mixture was left at room temperature for 5 min and then centrifuged (12,000 rpm, 4 °C) for 10 min. Next, 400 μL of the upper aqueous phase was transferred to a new 1.5 mL RNase-free EP tube, and 400 μL of pre-chilled isopropanol (4 °C) was added. The mixture was then mixed upside down and left at −20 °C for 20 min, and then the mixture was then centrifuged again (12,000 rpm, 4 °C) for 10 min. 1.0 mL of 75% ethanol was added after the supernatant was removed, and mixed upside down. Subsequently, the mixture was centrifuged (12,000 rpm, 4 °C) for 5 min and the supernatant was removed. The sample was air dried at room temperature for 5–10 min to allow the residual ethanol to evaporate. After that, 50 uL of DEPC water was added, and the RNA concentration was determined before reverse transcription. The reverse transcription was carried out by the FOREGENE reverse transcription kit (RT OR-EasyTM II) with a 20 μL reaction system and primers as indicated in Table S1. The expression levels of target genes were quantified using the comparative CT($2^{-\Delta\Delta CT}$) method, and normalized to GAPDH. The data were analyzed using GraphPad software (GraphPad Prism 8, La Jolla, CA, USA). Each step was performed three times independently to ensure minimal bias.

2.13. The mineralization of tooth slices in vitro

The tooth slices preserved in 0.1% Thymol solution were oven-dried (37 °C) for 12 h. Subsequently, 10 μL of each of the pastes was applied to one side of the tooth slices where the dentin tubules were exposed. The tooth slices were then immersed in a centrifuge tube containing 40 mL of simulated saliva and were shaken (100 rpm, 37 °C) for 3, 7, and 14 days, and the mineralization on the surface and cross-section of the tooth slices was observed and recorded. The thickness of the mineralized layers (T) was calculated and analyzed by the following formula (1):

$$T = \frac{1}{9}\sum_{i=1}^{i=9} T_i$$

T_i represented the thickness of any mineralized layer, three mineralized layer thickens were measured for each tooth slice, and three parallel samples were set up for each group.

2.14. Statistical analysis

All data were expressed as mean ± standard deviation (SD). Differences between groups were analyzed by ANOVA and Tukey's multiple comparison test. Statistically significant was considered when $p < 0.05$

(* means $p < 0.05$, ** means $p < 0.01$, *** means $p < 0.001$, **** means $p < 0.0001$).

3. Results and discussion

3.1. Characterization of samples

As illustrated in Fig. 2A, the heights of powders of equal mass of Monetite ($CaHPO_4$), S-Zn-β-TCP, and B-Zn-β-TCP in anhydrous ethanol were observed after 0, 15 min, and 6 h of static settling. The results indicated that at the starting point, the heights of the samples in anhydrous ethanol were consistent. However, after 15 min and 6 h of static settling, the heights of Monetite, S-Zn-β-TCP, and B-Zn-β-TCP in anhydrous ethanol gradually decreased, which was related to the particle sizes of these samples. Previous studies have shown that larger particles tend to settle faster compared to smaller particles [35]. As shown in Fig. 2B, Monetite exhibited a rod-like structure, with dimensions approximately measuring 150 nm in length and 20 nm in width, while S-Zn-β-TCP and B-Zn-β-TCP presented distinct square structures, with edge lengths of approximately 500 nm and 1 μm, respectively. The introduction of Zn^{2+} resulted in the transformation of monetite into the β-TCP phase, accompanied by a morphological change from rod-shaped nanoparticles to square-shaped particles. Gomes et al. have confirmed that Zn^{2+} can stabilize β-TCP [36]. The Energy Dispersive X-ray Spectroscopy (EDS) analysis revealed a uniform distribution of Zn on the surface of B-Zn-β-TCP, as demonstrated in Fig. 2C. Concurrently, the phase analysis results indicated that in the absence of Zn^{2+} doping, the sample primarily consisted of monetite, however, with the introduction of Zn^{2+}, a significant phase transformation occurred, shifting the main phase from monetite to β-TCP, while a minor amount of scholzite [$CaZn_2(PO_4)_2{\cdot}2H_2O$] was also formed, as illustrated in Fig. 2D. Many studies have demonstrated the stabilizing effect of Zn^{2+}on β-TCP [37–39]. Moreover, prior studies have indicated the biocompatibility and antibacterial properties associated with scholite [40,41]. In comparison to S-Zn-β-TCP, B-Zn-β-TCP revealed a higher proportion of the monetite phase, this discrepancy could be attributed to the synthetic process of S-Zn-β-TCP, wherein a larger quantity of ammonia was introduced. Consequently, this led to a reaction between OH^- and HPO_4^{2-} to form PO_4^{3-} and H_2O, thereby driving the transformation of monetite into β-tricalcium phosphate [42]. When the concentration of OH^- increased, the transformation rate of monetite to β-TCP was faster, so S-Zn-β-TCP possessed a smaller size compared to B-Zn-β-TCP. Without high temperature treatment, the main phase of Monetite was monetite, while the main phase of S-Zn-β-TCP and B-Z-β-TCP was Brushite ($CaHPO_4{\bullet}2H_2O$), as shown in Fig. S1. Dpsen et al. have confirmed that $CaHPO_4{\bullet}2H_2O$ was gradually transformed into $CaHPO_4$ after high temperature treatment, which led to the release of chemically bound water [43]. In addition, high temperature treatment was beneficial to the formation of PO_4^{3-} and H_2O from the reaction of HPO_4^{2-} and OH^-, and provided energy for Zn^{2+} to enter the β-TCP lattice gap to stabilize the β-TCP phase [36,42].

As shown in Fig. 2E, Fourier-transform infrared spectroscopy (FTIR) analysis was employed to investigate the chemical structures of Monetite, S-Zn-β-TCP, and B-Zn-β-TCP. Notably, the broad peak observed in the range of 3700 to 2500 cm^{-1} corresponded to the stretching vibration of H—O bonds of water molecules adsorbed on the sample surface. Additionally, the broad peak in the range of 1639 cm^{-1} indicated the bending vibration of H—O bonds in water molecules. The characteristic

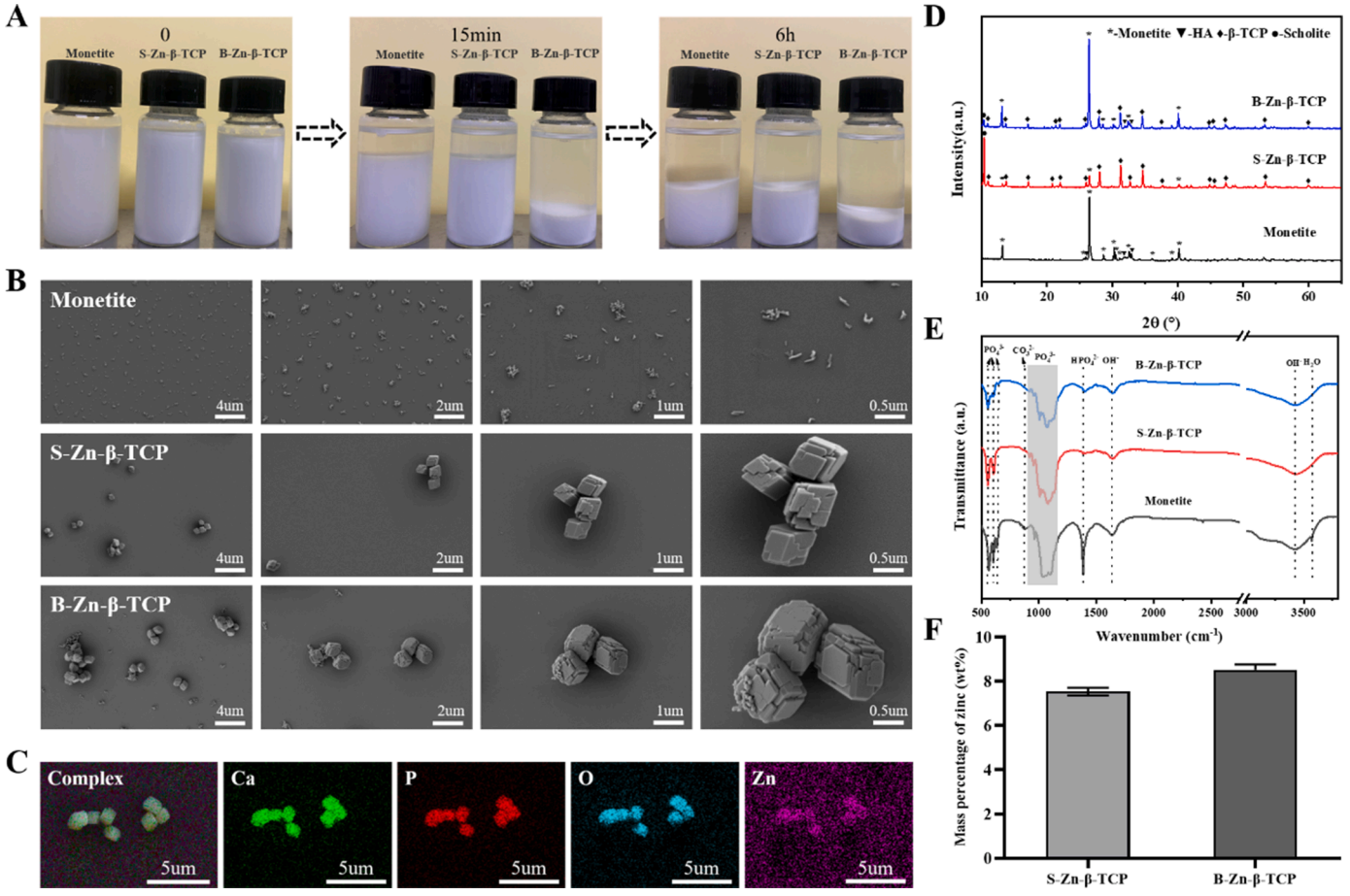

Fig. 2. The characterization of Monetite, S-Zn-β-TCP, and B-Zn-β-TCP. (A) Samples of equal mass were placed in anhydrous ethanol for 15 min and 6 h; (B) SEM images; (C) EDS mapping; (D) XRD spectra; (E) FTIR spectra; (F) ICP-MS.

peak of CO_3^{2-} at 872 cm^{-1} indicated the presence of CO_3^{2-} in the doped samples, leading to the formation of a minor quantity of carbonate apatite [44]. Importantly, the substitution of CO_3^{2-} did not affect the biological functionality of samples. On the contrary, previous research has demonstrated that the combination of carbonate apatite and HA exhibited better biocompatibility than pure HA, as carbonate apatite was naturally found in human bones [45]. Further analysis of the FTIR spectra revealed a broad peak at 1380 cm^{-1}, which corresponded to the in-plane bending of P-O-H, while a peak at 639 cm^{-1} was attributed to the bending vibration of PO_4^{3-} in HA [46]. Moreover, peaks at 560 cm^{-1} and 605 cm^{-1} were assigned to the bending vibration of PO_4^{3-} in β-TCP and HA, respectively, while the shaded regions at 958 cm^{-1}, 1034 cm^{-1}, 1108 cm^{-1}, 968 cm^{-1}, 1020 cm^{-1}, and 1120 cm^{-1} were associated with the stretching vibration of PO_4^{3-} in β-TCP and HA [47,48]. The peaks at 1090 cm^{-1} and 1027 cm^{-1} were attributed to the stretching vibration of PO_4^{3-} in monetite [48].

The above results showed that the phase and chemical structure of the main phase monetite and β-TCP, as well as the secondary phase HA and scholzite could correspond to other research results. In addition, quantitative analysis of Zn^{2+} content in S-Zn-β-TCP and B-Zn-β-TCP was conducted by ICP-MS, and the results indicated that B-Zn-β-TCP exhibits a higher Zn^{2+} content compared to S-Zn-β-TCP, as illustrated in Fig. 2F. A previous study has suggested that the interaction between Zn^{2+} and ammonia led to the formation of zinc ammonia complex ions [$Zn(NH_3)_4^{2+}$]. Consequently, some Zn^{2+} remained in the solution and did not precipitate, resulting in a lower overall Zn^{2+} content in the calcium phosphate matrix [49]. The concentration of Zn^{2+} in the supernatant before and after the high-temperature reaction was shown in Fig. S2. The results showed that the concentration of Zn^{2+} in B-Zn-β-TCP supernatant was all higher than those of S-Zn-β-TCP. Before reacted, the concentration of Zn^{2+} in the supernatant of S-Zn-β-TCP lower than that of B-Zn-β-TCP, which was attributed to the higher amount of ammonia added for the preparation of S-Zn-β-TCP, and the concentration of [$Zn(NH_3)_4^{2+}$] in the supernatant of S-Zn-β-TCP was higher than that of B-Zn-β-TCP. After the reaction, the concentration of Zn^{2+} in the supernatant of S-Zn-β-TCP and B-Zn-β-TCP increased significantly, which attributed to the transformation of $CaHPO_4 \bullet 2H_2O$ to β-TCP, the doping rate of Zn^{2+} in β-TCP (High-temperature phase) was lower [36]. Given the high amount of ammonia was added in preparation of the S-Zn-β-TCP, the situation that Zn^{2+} in the supernatant of B-Zn-β-TCP was higher than that of S-Zn-β-TCP did not change.

3.2. *The mineralization evaluation of Monetite, S-Zn-β-TCP, and B-Zn-β-TCP in vitro*

To evaluate the *in vitro* mineralization ability and bioactivity of samples, the simulated body fluid (SBF) can be employed to pre-test the *in vitro* formation of HA [50]. The equal masses of Monetite, S-Zn-β-TCP, and B-Zn-β-TCP were immersed separately in equal volumes of simulated saliva and SBF, and the formation and rate of HA on the sample surfaces were observed. The results demonstrated that compared with the pre-mineralization (Fig. 2B), both S-Zn-β-TCP and B-Zn-β-TCP exhibited rod-shaped nanoparticles adhering to the surface with some aggregation after mineralization, while Monetite showed significant aggregation (Fig. 3A). Since the mineralization product was rod-shaped nanoparticles, the mineral deposited on Monetite could not be clearly observed. During immersion in simulated saliva, all three samples (Monetite, S-Zn-β-TCP, and B-Zn-β-TCP) gradually released Ca^{2+}, Zn^{2+}, and PO_4^{3-} from their surfaces, these released ions facilitated nucleation and subsequent surface mineralization. The locally higher concentrations of mineralization-promoting ions released between particles created favorable conditions for crystallization, leading to the formation of mineralized layers. These mineralized layers played a crucial role in connecting adjacent particles, thereby resulting in aggregation phenomena [51]. The mineral phases and chemical structures of Monetite, S-Zn-β-TCP, and B-Zn-β-TCP after mineralization were investigated using XRD and FTIR. The results revealed that the induced mineral formed during the mineralization process was HA, with the corresponding functional groups being detectable, as shown in Fig. S3. These outcomes were consistent with the findings of Tan et al. [52]. However, it was observed that the mineralization effects of samples in the SBF were relatively poor, as shown in Fig. 3B. After 4 days of mineralization, the Monetite group remained dispersed, and the surfaces of S-Zn-β-TCP and B-Zn-β-TCP exhibited almost no mineral deposits. After 7 days of mineralization, the Monetite group showed some degree of aggregation, and the surfaces of S-Zn-β-TCP and B-Zn-β-TCP displayed fine and uniform mineral deposits. Notably, no mineral deposits were observed in any of the samples after just 1 day of mineralization (data not shown).

These results suggested that the mineralization effect of Monetite, S-Zn-β-TCP, and B-Zn-β-TCP in simulated saliva was superior to that in SBF, which could be attributed to the differences in composition between simulated saliva and SBF. Specifically, the concentration of HPO_4^{2-} in simulated saliva was approximately five times that in SBF, while the concentration of Ca^{2+} was not significantly different (Tables S2 and S3). Research conducted by Tan et al. has confirmed that biphasic calcium phosphate exhibited better mineralization effects in simulated saliva when compared to SBF [52]. The β-TCP were mineralized in AS and SBF respectively for 14 days, and the effect of inducing mineral deposition on the surface of β-TCP was observed, as shown in Fig. S4. The results showed that mineral deposited on the surface of β-TCP particles in both AS and SBF, and the effect of β-TCP on mineralization induction in AS was similar to that of S-Zn-β-TCP and B-Zn-β-TCP, but the effect of β-TCP on mineralization induction in SBF was better those of them. It has been confirmed that Zn^{2+} could inhibit the mineralization effect of apatite in SBF [53]. Moreover, it has been shown that Ca^{2+}, PO_4^{3-}, and other ions dissolved from calcium phosphate in the neutral environment were not only related to the formation of HA on the calcium phosphate surface and its chemical bonding with bone but also played a crucial role in gene activation [54]. Therefore, it was essential to investigate the ion dissolution behavior of Monetite, S-Zn-β-TCP, and B-Zn-β-TCP *in vitro*, which could provide a reference for the potential application of Zn-β-TCP in the fields of bone and dental repair. During the mineralization process, the concentrations of Ca^{2+} and Zn^{2+} in the simulated saliva, in which Monetite, S-Zn-β-TCP, and B-Zn-β-TCP were immersed, exhibited a notable pattern of initial increase followed by subsequent decrease, as illustrated in Fig. 3C. An initial increment could be attributed to as mineralization progressed, the samples initially dissolved and released Ca^{2+} and Zn^{2+}, leading to an increment in their concentrations. Subsequently, during the recrystallization to form mineral deposits, the concentrations of Ca^{2+} and Zn^{2+} decreased, which aligned with the findings of Tan et al. [52]. Significantly, the concentration of Ca^{2+} and Zn^{2+} released from B-Zn-β-TCP was higher than that of S-Zn-β-TCP, probably due to differences in the phase composition between B-Zn-β-TCP and S-Zn-β-TCP. The related studies have demonstrated that, in comparison to pure Zn-β-TCP, Zn-doped monetite dissolved more readily and released higher amounts of Ca^{2+} and Zn^{2+} [55]. The pH values in the supernatant of AS and SBF after the mineralization were tested and the results were shown in Fig. S5. The results showed that the pH value in the supernatant of AS and SBF does not change significantly during the mineralization process. The pH value in the supernatant of SBF after mineralization was higher than that of AS because the pH value of the SBF stock was higher than that of AS. Due to the dissolution of $CaHPO_4$ in AS and the release of HPO_4^{2-}, HPO_4^{2-} reacted with OH^- to produce H^+, PO_4^{3-}, and H_2O which led to the increase of H^+ concentration in AS and the decrease of pH value, resulting in the pH value of the supernatant of Monetite mineralized in AS being lower than those of other groups. Therefore, the pH value of the supernatant of the Monetite decreased after mineralization in AS.

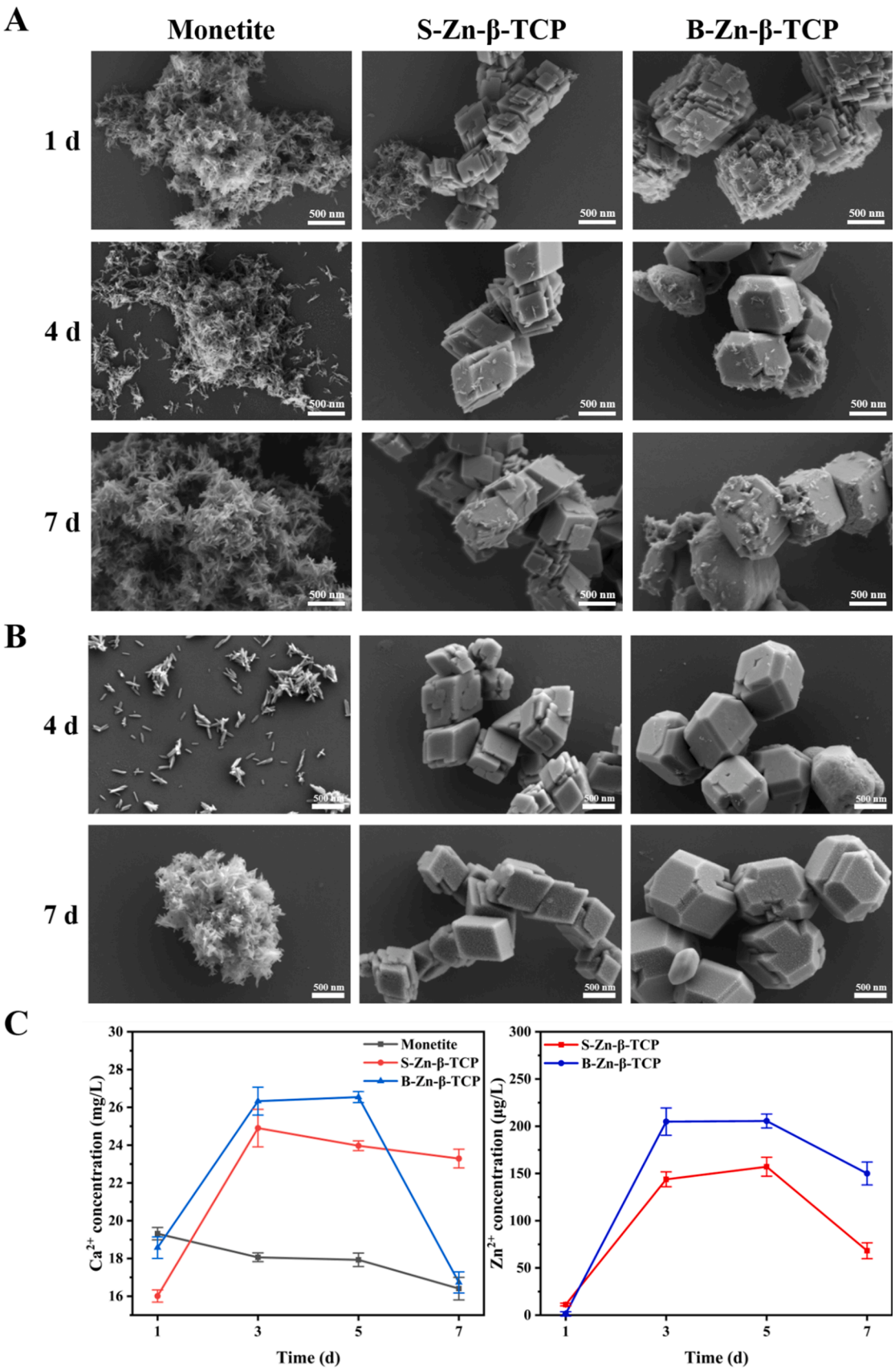

Fig. 3. The mineralization evaluation *in vitro*. (A) SEM images of samples mineralized in simulated saliva for 1, 4, and 7 days; (B) SEM images of samples mineralized in simulated body fluid for 4 and 7 days; (C) The changes of Ca^{2+} and Zn^{2+} concentrations in simulated saliva. ($n = 3$).

3.3. The biocompatibility evaluation of samples in vitro

The biocompatibility of Monetite, S-Zn-β-TCP, and B-Zn-β-TCP was assessed by co-culturing their ion leachates with primary rat DPSCs and rat BMSCs. The results displayed that, as the culturing time increased, the number of cells in each group gradually increased, and no significant differences were observed among them (Fig. 4A). However, the S-Zn-β-TCP and B-Zn-β-TCP showed a more pronounced promotion of DPSCs proliferation compared to the Monetite, indicating that the addition of Zn^{2+} was beneficial to the proliferation of DPSCs. The live/dead staining results further confirmed the excellent biocompatibility of all three samples, as no dead cells were observed in each group after 7 days of culture (Fig. 4B). Additionally, the S-Zn-β-TCP and B-Zn-β-TCP showed more pronounced cell spreading compared to both the control group and the Monetite. Notably, the B-Zn-β-TCP demonstrated the most significant cell spreading, which can be attributed to the higher concentration of Zn^{2+} in B-Zn-β-TCP. Previous studies have demonstrated that Zn^{2+} played a crucial role in promoting the proliferation of DPSCs [56,57].

To further validate the biocompatibility of Monetite, S-Zn-β-TCP, and B-Zn-β-TCP, the ion leachates of samples were co-cultured with rat MSCs. The cell numbers in all groups increased with prolonged culturing time, and the cell numbers in the S-Zn-β-TCP and B-Zn-β-TCP were higher than those of the Monetite. After 3 days and 5 days of culture, the cell numbers in the S-Zn-β-TCP and B-Zn-β-TCP exhibited a significant increase compared to the control group and Monetite (Fig. 5A). On the 7th day, the live/dead staining results demonstrated no cell death in any group, consistent with the findings from the DPSCs. Moreover, the green fluorescence density in the S-Zn-β-TCP and B-Zn-β-TCP was higher than that in the control group and Monetite (Fig. 5B). Many studies have confirmed that Zn^{2+} played a significant role in promoting the proliferation of MSCs [58]. In comparison to pure β-TCP, Zn-doped β-TCP could significantly enhance both the proliferation and differentiation of MSCs [55]. Taken together, these results suggested that Monetite, S-Zn-β-TCP, and B-Zn-β-TCP all exhibited excellent biocompatibility. In addition, the inclusion of Zn^{2+} in β-TCP positively influenced their biocompatibility, particularly in terms of cell proliferation and spreading.

3.4. The evaluation of odontoblast differentiation of Monetite, S-Zn-β-TCP, and B-Zn-β-TCP in vitro

DPSCs were known for their multipotent differentiation characteristics and were considered a promising source for dental pulp regeneration. Certain markers such as OCN (osteocalcin), OPN (osteopontin), DSPP (dentin sialophosphoprotein), BSP (bone sialoprotein), and DMP1 (dentin matrix acidic phosphoprotein 1) were recognized as dental-specific differentiation markers for DPSCs [59,60]. Typically, OCN is found in bone and dentin and plays a regulatory role in hard tissue mineralization. The production of OCN is limited to cells with mineralization functions, including osteoblasts, endodontoblasts, and

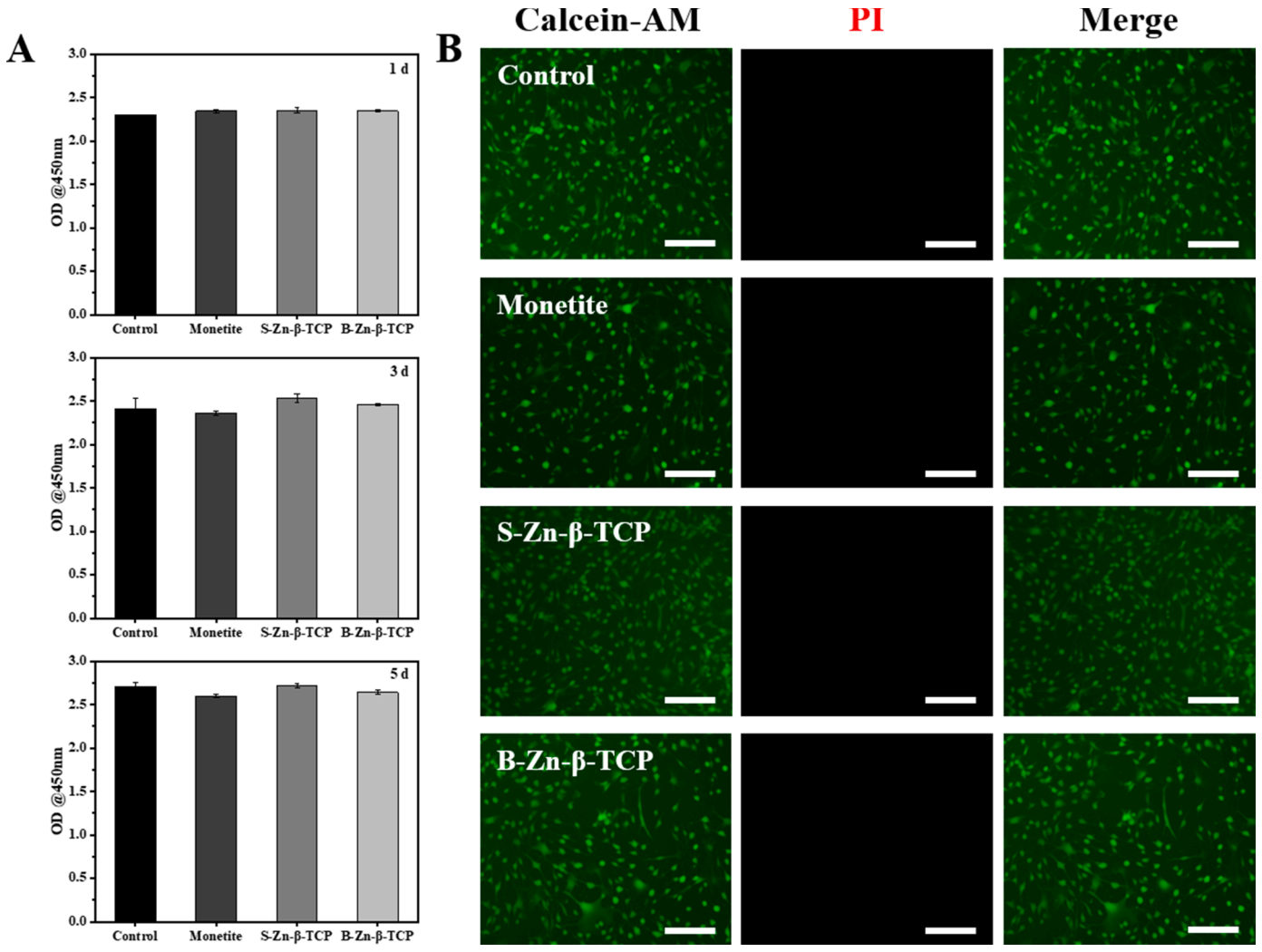

Fig. 4. The biocompatibility evaluation of dental pulp stem cells *in vitro*. (A) OD values of DPSCs after culturing with sample extracts for 1, 4, and 7 days; (B) The live/dead staining of DPSCs after culturing with sample extracts for 7 days; scale bar=200 μm. ($n = 3$, $^*p < 0.05$).

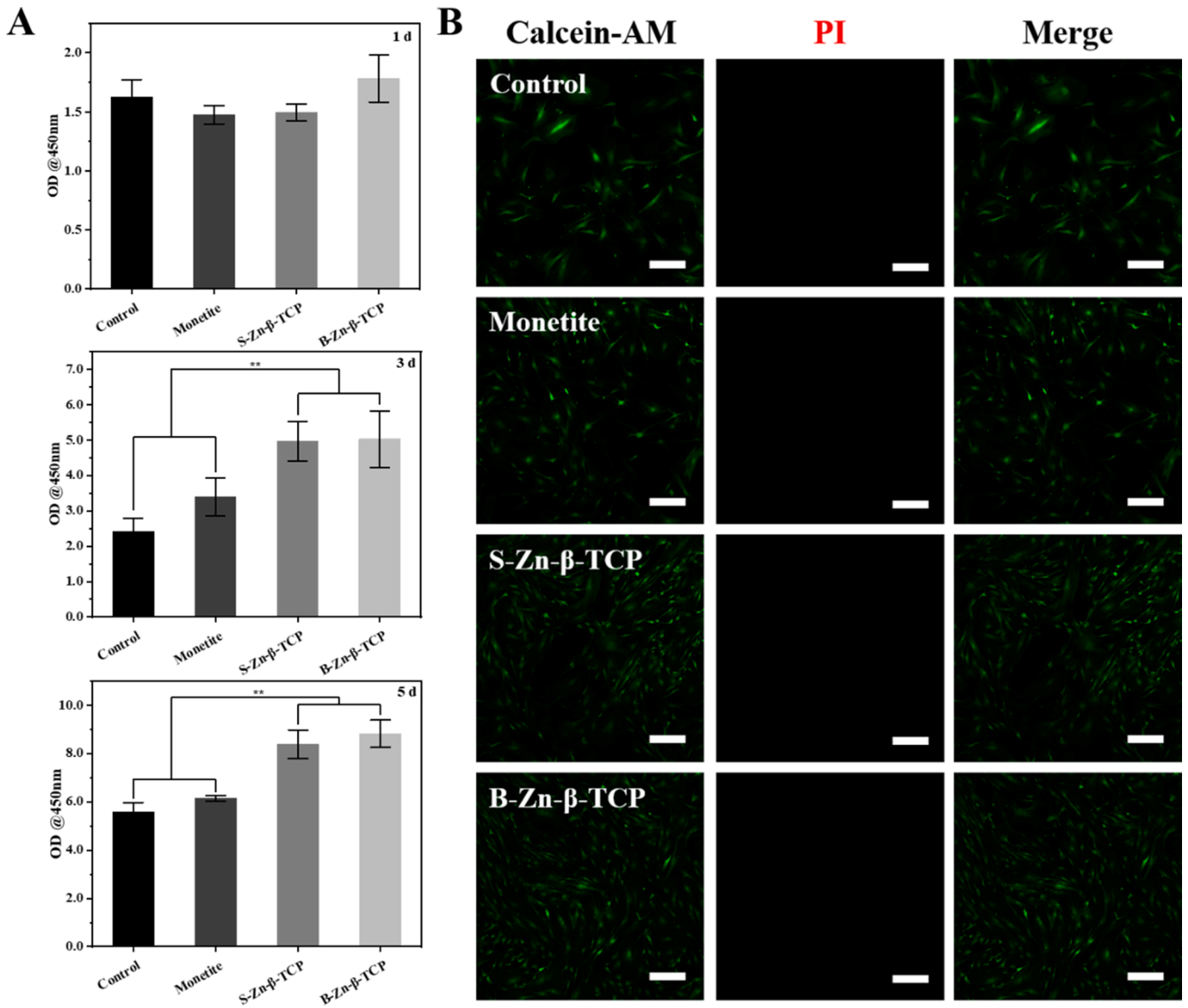

Fig. 5. The biocompatibility evaluation of BMSCs *in vitro*. (A) OD values of BMSCs after culturing with sample extracts for 1, 4, and 7 days; (B) The live/dead staining of BMSCs after culturing with sample extracts for 7 days; scale bar=200 μm. ($n = 3$, $^*p < 0.05$).

cementoblasts, and the mineralization-promoting ability of DPSCs is closely related to the expression level of OCN [61]. Although OPN has bone-related functions, it is not bone-specific and is usually involved in the repair of mineralized tissue, in the case of restorative dentin, OPN plays a role in the initial formation and mineralization of this tissue [62]. DSPP is one of the markers of odontogenic differentiation, and the expression level of DSPP increases gradually with the progression of induced differentiation. DSPP is also one of the essential proteins for normal tooth development and plays a crucial role in the process of dentin formation after the formation of dentin matrix [63]. DMP1 is an extracellular matrix protein that participates in the differentiation of DPSCs into odontoblasts. DMP1 is considered to play a key biological role in the mineralization of bone and dentin. It is reported that DMP1 exists in all stages of tooth development and plays an important role in dentin differentiation of dental pulp stem cells [62]. To evaluate the potential of Monetite, S-Zn-β-TCP, and B-Zn-β-TCP in promoting dental-specific differentiation, the expression levels of OCN, BSP, DSPP, and DMP-1 in DPSCs were examined, as shown in Fig. 6. Among these samples, S-Zn-β-TCP demonstrated the highest expression levels of BSP and OCN. Although the expression levels of BSP and OCN in the B-Zn-β-TCP were not as high as those of the S-Zn-β-TCP, they still exhibited higher expression levels compared to the control group. Previous studies have highlighted the importance of maintaining an appropriate concentration of Zn^{2+} to promote the expression of BSP and OCN in DPSCs, as excessive Zn^{2+} can inhibit their expression [56]. However, the expression levels of DSPP and DMP-1 in the Monetite and S-Zn-β-TCP were significantly lower than in the control group and the B-Zn-β-TCP, which may be related to the high concentration of Ca^{2+}. Mizumachi et al. have demonstrated that excessive Ca^{2+} could inhibit the expression of DSPP and DMP-1 in DPSCs [64]. Furthermore, the expression levels of DSPP and DMP-1 in the Monetite, S-Zn-β-TCP, and B-Zn-β-TCP exhibited a sequential increase, indicating that the presence of Zn^{2+} can promote the expression of DSPP and DMP-1, which was consistent with the findings of Huang et al. [56]. Overall, these results suggested that an appropriate concentration of Zn^{2+} could play a promoting role in dentin-like differentiation, while excessively high concentrations of both Ca^{2+} and Zn^{2+} were not conducive to the dentin-like differentiation of DPSCs. Therefore, maintaining an optimal balance of ions, particularly Zn^{2+} and Ca^{2+}, was beneficial to the successful dental-specific differentiation of DPSCs.

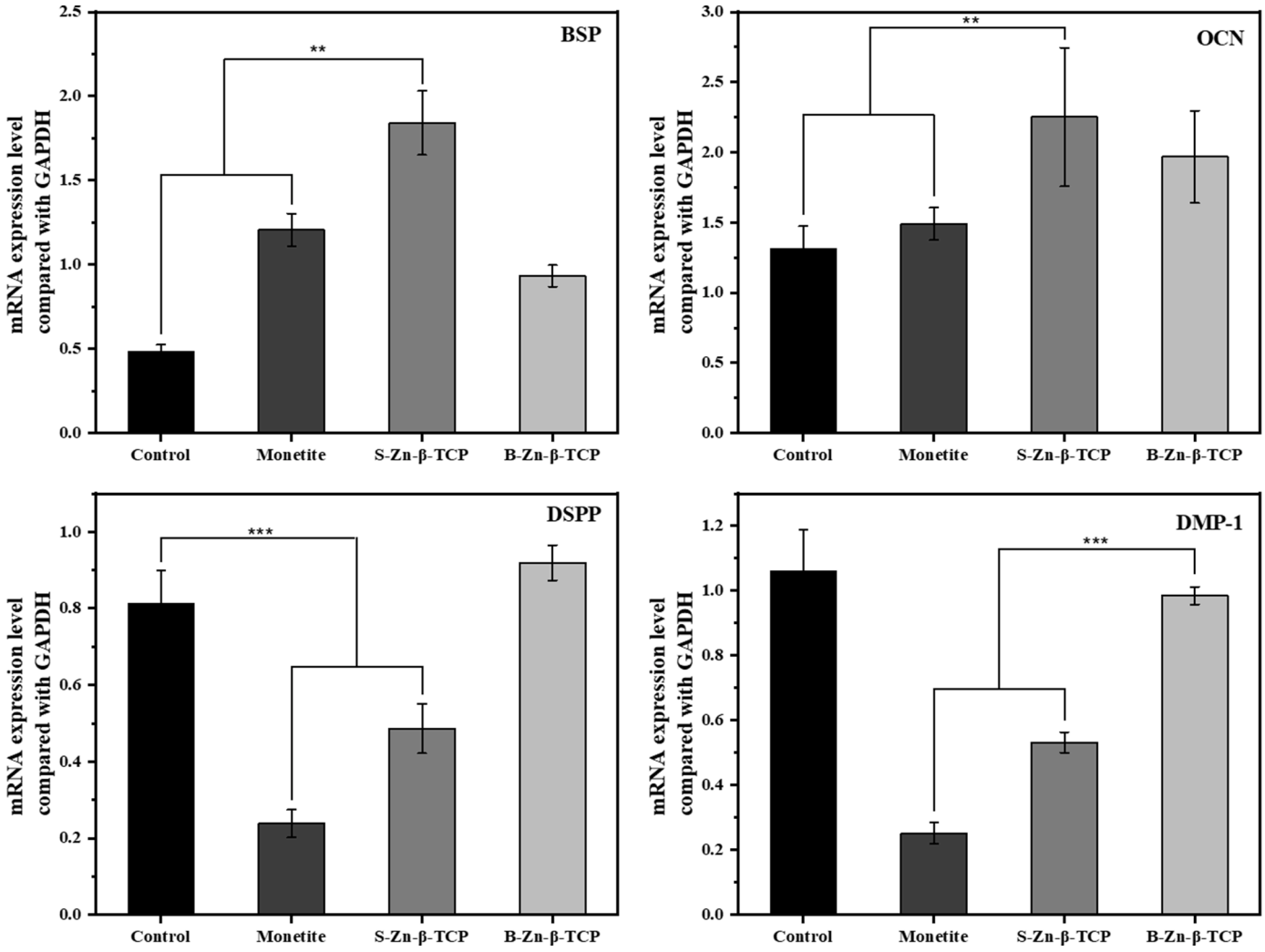

Fig. 6. The expression of BSP, OCN, DSPP, and DMP-1 in dental pulp stem cells after culturing with sample extracts for 5 days. ($n = 3$, $^*p < 0.05$).

3.5. The antibacterial activity evaluation of Monetite, S-Zn-β-TCP, and B-Zn-β-TCP in vitro

Dentin hypersensitivity was primarily caused by the demineralization of tooth enamel and dentin. Food residues adhered to the tooth enamel surface could undergo bacterial fermentation, leading to the production of acidic substances that corrode both enamel and dentin, constituting a significant factor in dentin hypersensitivity [65]. Although various oral bacteria were present in the oral cavity, only a few microbial strains were suspected to play a role in promoting dentin hypersensitivity. Streptococcus mutants, in particular, possessed the capability to respond to various stresses during host acquisition and biofilm formation. As a result, it released substantial amounts of lactic acid upon fermenting dietary carbohydrates, which led to tooth etching and demineralization [66,67]. Antibacterial abilities were an essential feature for materials used to treat dentin hypersensitivity to fight harmful bacteria effectively. The antibacterial feature was crucial in preventing further deterioration of tooth structure and promoting the restoration of dental health in patients with dentin hypersensitivity. The antibacterial capabilities of the Monetite, S-Zn-β- TCP, and B-Zn-β-TCP were thoroughly evaluated through co-culturing leachates with Streptococcus mutants and agar diffusion test, as shown in Fig. 7. The results demonstrated that after 12 h of co-culturing, the OD value of the S-Zn-β-TCP was the lowest, while the Monetite exhibited the highest OD value. The OD value of the Monetite showed significant differences compared to the control group, S-Zn-β-TCP, and B-Zn-β-TCP, whereas the OD values of the control groups, S-Zn-β-TCP and B-Zn-β-TCP were similar. After 24 h of co-culturing, the OD value of the B-Zn-β-TCP was the lowest, and the Monetite continued to have the highest OD value. The OD value of Monetite still exhibited significant differences compared to the control group, S-Zn-β-TCP, and B-Zn-β-TCP. However, the OD values of S-Zn-β-TCP and B-Zn-β-TCP already showed significant differences compared to the control group (Fig. 7A). These findings suggested that a certain concentration of Ca^{2+} promoted the proliferation of Streptococcus mutants, while Zn^{2+} exhibited an excellent antibacterial effect against Streptococcus mutants. Moreover, Spengler et al. demonstrated that saliva enhanced the adhesion of Streptococcus mutants to HA, primarily due to the abundant presence of Ca^{2+} in saliva [68]. Additionally, Zhou et al. reported that Ca^{2+} promoted the adhesion and proliferation of Streptococcus mutants by mediating the surface protein P1, thereby facilitating the occurrence and progression of dental caries [69]. Conversely, Zn^{2+} showed remarkable antibacterial effects against Streptococcus mutants, corroborating with many studies [70, 71]. Furthermore, Liu et al. have shown that BioUnion fillers could induce the release of Zn^{2+} under acidic conditions, leading to the inhibition of Streptococcus mutans [71]. The results of the co-coated plate method were consistent with the trends of co-culturing for 24 h, with the Monetite exhibiting the highest number of colonies, and the S-Zn-β-TCP and B-Zn-β-TCP showing fewer colonies (Fig. 7B). The quantification of colony numbers aligned with the co-culturing outcomes, as illustrated in Fig. S6. Collectively, these findings indicated that the S-Zn-β-TCP and B-Zn-β-TCP exhibited the most effective antibacterial effects among the

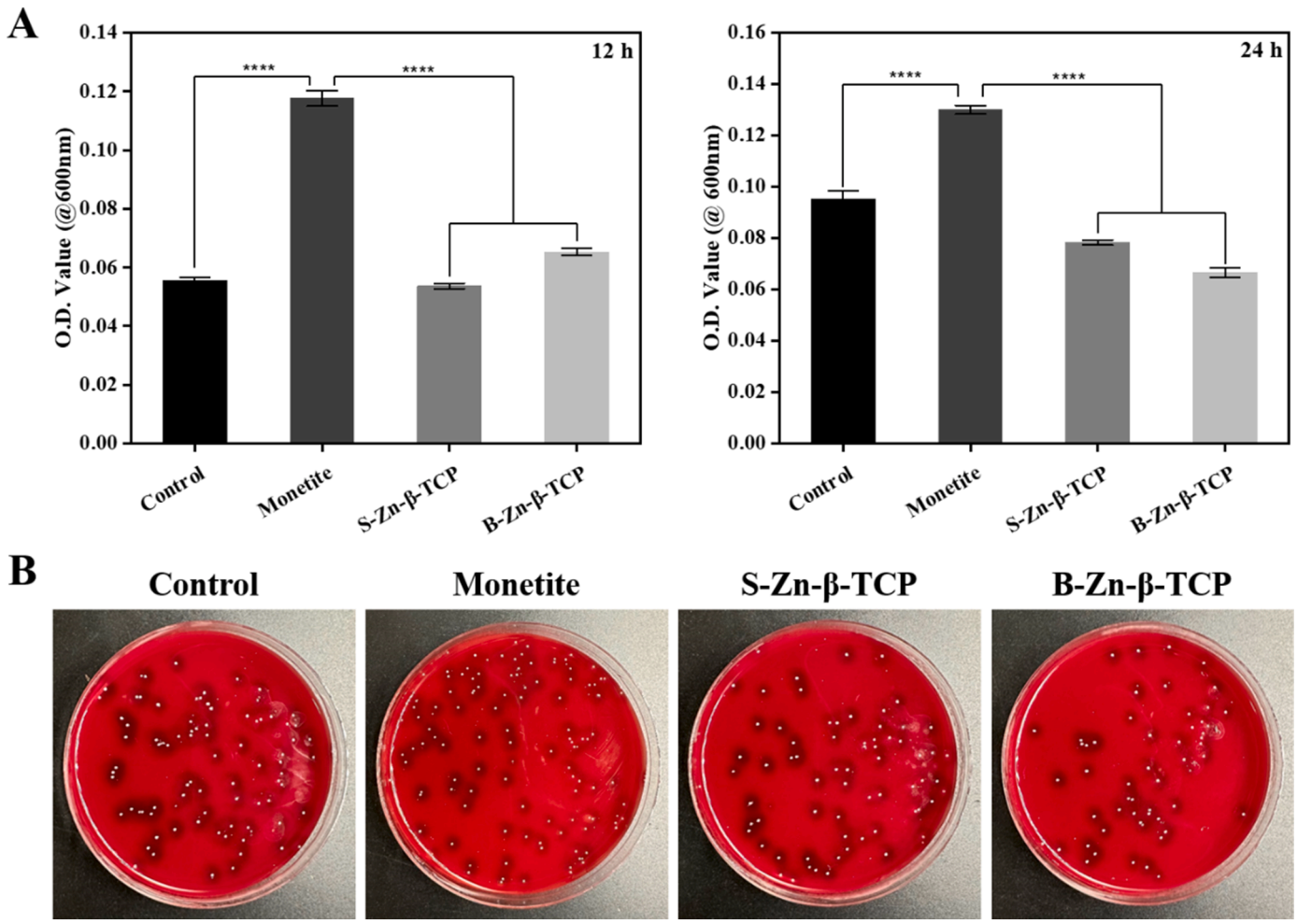

Fig. 7. The antibacterial evaluation of sample extracts *in vitro*. (A) OD values of sample extracts incubated with Streptococcus mutants after 12 and 24 h; (B) Photographs of sample extracts co-cultured with Streptococcus mutants for 24 h. ($n = 3$, $^*p < 0.05$).

groups.

3.6. Preparation of tooth slices and the viscosity evaluation of pastes in vitro

The human third molars were collected and cut into dimensions of 5 × 5 × 1 mm, as shown in Fig. 8A. During the polishing process, the tooth slices underwent debris generation, which sealed off the dentinal tubules, leaving them unexposed, as indicated by the red arrows in Fig. 8B. Following acid etching, the tooth slices exhibited clear dentinal tubules, and the side view revealed that the dentinal tubules were unblocked (Fig. 8C). The exposed dentinal tubules were measured to be approximately 4 um, which was consistent with previous studies [32]. Considering the constant exposure of teeth to the moist oral environment and daily consumption of food and water, dental materials needed to possess a certain viscosity, which could ensure firm adhesion to the tooth surface [72]. The image of S-Zn-β-TCP/SA/PEG paste was shown in Fig. 9A, and S-Zn-β-TCP/SA/PEG paste could glue the separated tooth slices together, as shown in Fig. 9B, demonstrating the excellent viscosity of S-Zn-β-TCP/SA/PEG. To further assess the binding strength of the paste on the tooth surface, S-Zn-β-TCP/SA and S-Zn-β-TCP/SA/PEG were separately applied to the tooth grooves, followed by water flushing, as shown in Movie S1 and Movie S2. Photographs were taken to record the residue of paste on the tooth groove surface before and after flushing, as illustrated in Fig. 9C. The above results revealed that the S-Zn-β-TCP/SA on the tooth groove was completely washed away after flushing, whereas a lot of S-Zn-β-TCP/SA/PEG remained on the tooth groove, indicating the superior viscosity of S-Zn-β-TCP/SA/PEG compared to S-Zn-β-TCP/SA. Importantly, previous studies have shown that PEG-4000 not only possessed excellent viscosity but also exhibited excellent abilities to induce mineralization [73,74]. The incorporation of PEG-4000 significantly enhanced the adhesion between the paste and tooth groove in the current study.

3.7. The evaluation of paste-induced mineralization on tooth slices in vitro

The tooth slices treated with SA, Monetite/SA, S-Zn-β-TCP/SA, and B-Zn-β-TCP/SA underwent mineralization in simulated saliva for 7 days and 14 days, as shown in Fig. 10. The dentinal tubules were gradually covered by the mineralization layer, and the number of exposed dentinal tubules was reduced as the mineralization time could be observed. In the control group, SA, and Monetite/SA, the number of exposed dentinal tubules decreased over time. In contrast, dentinal tubules of the tooth slices treated with S-Zn-β-TCP/SA and B-Zn-β-TCP/SA were completely covered by the mineralization layer, as shown in Fig. 10A. Previous studies have indicated that sodium alginate could induce *in-situ* mineralization of calcium phosphate [22,75]. Additionally, on the 7th day of mineralization, almost no mineralized coating deposition was observed in the cross-sections of tooth slices from the control group, SA, and Monetite/SA. However, significant mineralized coating deposition was observed in the cross-sections of tooth slices from the S-Zn-β-TCP/SA and B-Zn-β-TCP/SA. Although the mineralized coating of the S-Zn-β-TCP/SA was thicker compared to the B-Zn-β-TCP/SA, it appeared

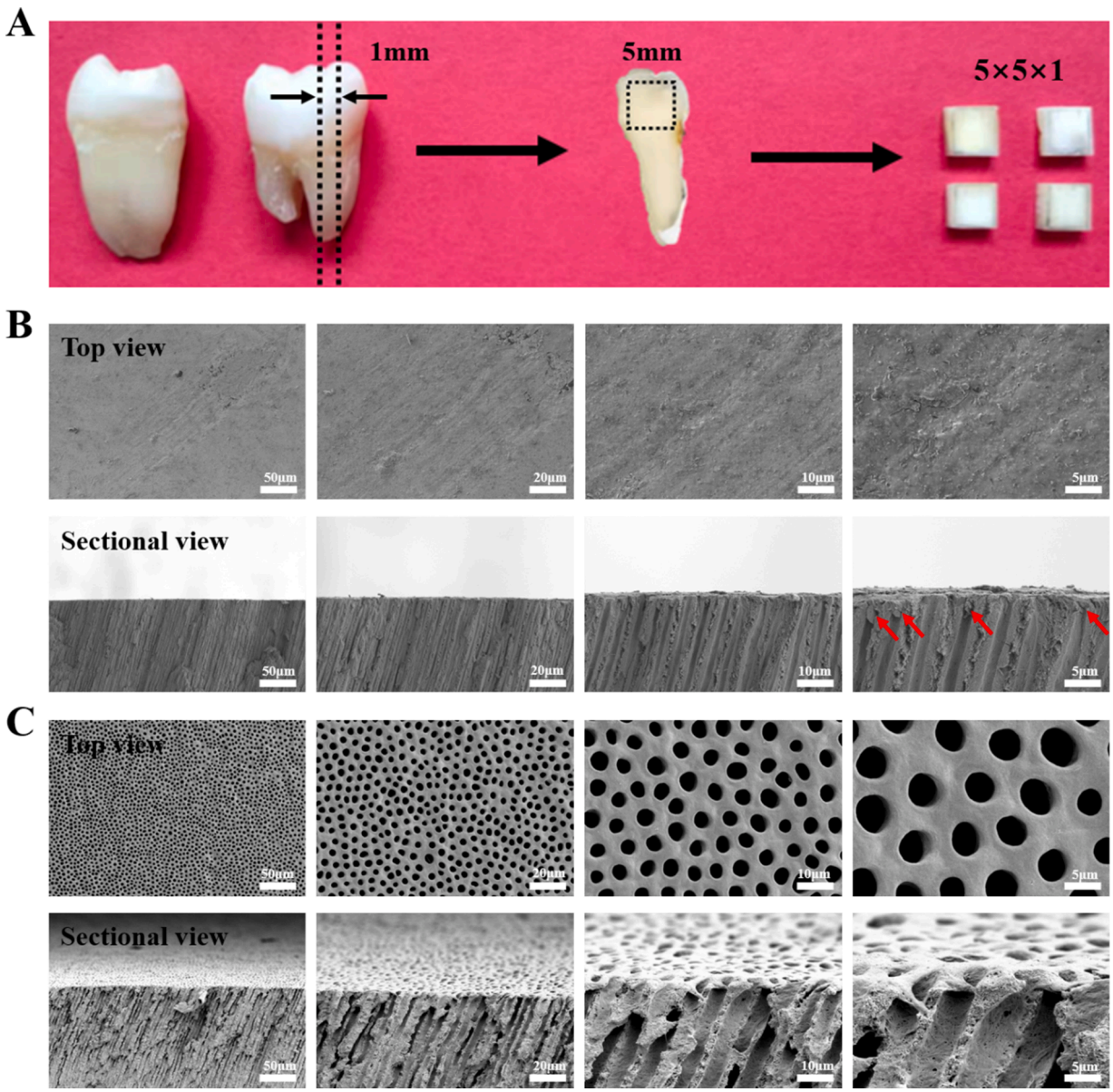

Fig. 8. Preparation of tooth slices. (A) Macroscopic images of tooth slices; (B) SEM image of the top and cross-sectional surfaces of tooth slice without acid etching; (C) SEM image of the top and cross-sectional surfaces of tooth slice with acid etching.

more porous and loosely bound to the tooth slices (Fig. 10A). Furthermore, in comparison to the control group and SA, the Monetite/SA exhibited a better mineralization-inducing effect, which could be attributed not only to the addition of Monetite but also to its role in mineralization induction [76]. After 14 days of mineralization, the cross-sections of tooth slices from the control group, SA, and Monetite/SA showed thin mineralized coating depositions, with the thickness of the mineralized coating increasing sequentially. The tooth slices from the S-Zn-β-TCP/SA and B-Zn-β-TCP/SA exhibited thick mineralized coatings on the surface. Notably, compared to 7 days of mineralization, the mineralized coating in the S-Zn-β-TCP/SA became denser after 14 days, with no distinct boundary between the coating and the slices, suggesting significant degradation of sodium alginate during the mineralization induction. Previous studies have shown that Ca^{2+} and Zn^{2+} could chelate with the carboxyl groups in sodium alginate, and that the uniformly dispersed mineralized phase could be formed by enzymatic induction [77,78]. However, the mineralized coating in the B-Zn-β-TCP/SA after 14 days was not as dense as that in the S-Zn-β-TCP/SA, which may be attributed to the larger particle size of B-Zn-β-TCP. Huang et al. have demonstrated that smaller-sized TCP performed better in closing gaps between teeth and composite materials, implying that smaller-sized TCP particles could be more effective in inducing mineralization to close gaps formed during the bonding process [79]. The measurement schematic diagram of the thickness of the mineralized layer on the dentin surface was shown in Fig. 10B. Quantitative analysis of the mineralized coating thickness revealed an increase in thickness in each group with the extension of mineralization time. The thickest mineralized coatings of Monetite/SA and B-Zn-β-TCP/SA were higher than those of the control group and SA (Fig. 10C). The S-Zn-β-TCP/SA exhibited the thickest mineralized coating, which was significantly different from that of the control group, SA, and Monetite/SA and B-Zn-β-TCP/SA. Taken together, the S-Zn-β-TCP/SA exhibited the superior mineralization-inducing ability in the tooth slices to occlude dentin tubules.

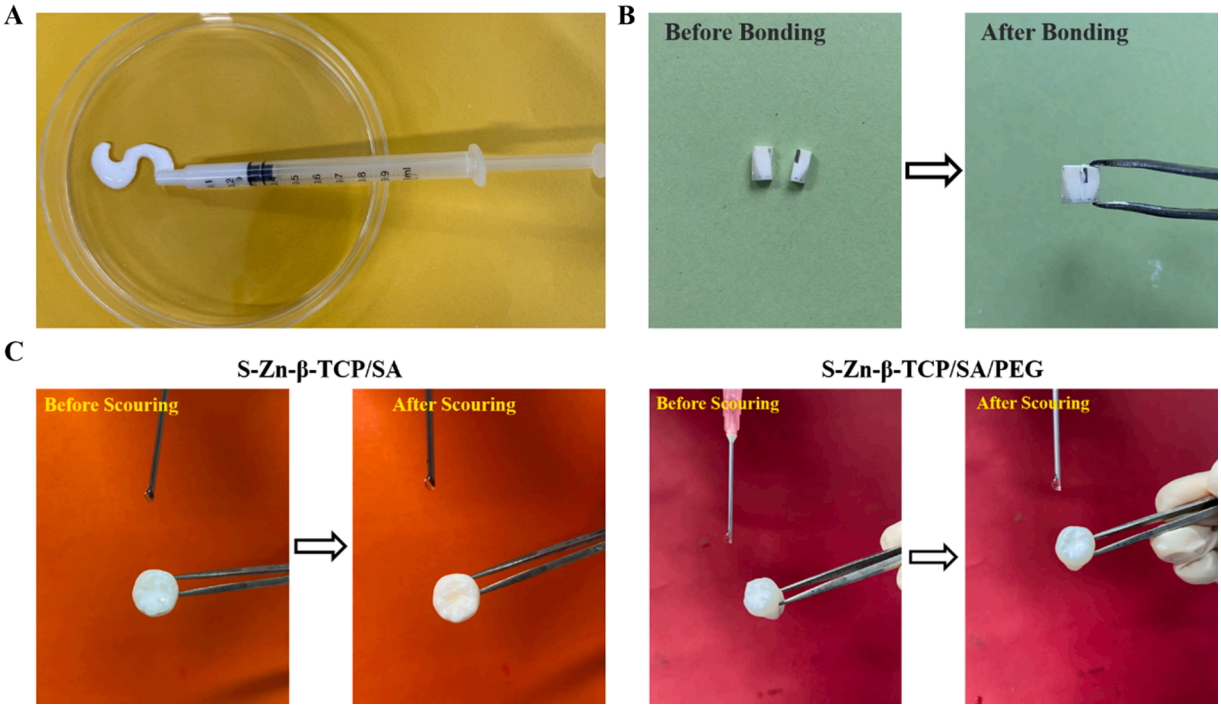

Fig. 9. The viscosity evaluation of the pastes *in vitro*. (A) Images of S-Zn-β-TCP/SA/PEG paste; (B) Images of S-Zn-β-TCP/SA/PEG paste adhering tooth slices; (C) Images of S-Zn-β-TCP/SA and S-Zn-β-TCP/SA/PEG on teeth after flushing by water flow, showing that a lot of S-Zn-β-TCP/SA/PEG remained adhering on the tooth groove while almost no S-Zn-β-TCP/SA on the tooth groove.

3.8. The evaluation of paste-induced mineralization on tooth slices in vitro

Based on the results from Section 3.7, the SA, Monetite/SA, and S-Zn-β-TCP/SA were selected to be combined with PEG-4000 to further enhance the mineralization induction effect and viscosity of the paste. The tooth slices treated with SA/PEG, Monetite/SA/PEG, and S-Zn-β-TCP/SA/PEG were mineralized in simulated saliva for 3, 7, and 14 days, as shown in Fig. 11. After 3 days of mineralization, the tooth slices treated with SA/PEG and Monetite/SA/PEG still exhibited many exposed dentinal tubules, whereas the Monetite/SA/PEG showed fewer exposed dentinal tubules than the SA/PEG, and those treated with S-Zn-β-TCP/SA/PEG had almost no exposed dentinal tubules. After 7 days of mineralization, the tooth slices coated with SA/PEG showed a few exposed dentinal tubules, while those treated with Monetite/SA/PEG had scattered dentinal tubules, the tooth slices treated with S-Zn-β-TCP/SA/PEG had no exposed dentinal tubules. After 14 days, none of the tooth slices coated with SA/PEG, Monetite/SA/PEG, and S-Zn-β-TCP/SA/PEG showed exposed dentinal tubules, as depicted in Fig. 11A. These findings indicated that the combination of PEG could effectively accelerate the formation of mineralized coatings, which was consistent with previous studies [80]. The quantification of the mineralized coating thickness revealed that the mineralized coating on tooth slices treated with SA/PEG, Monetite/SA/PEG, and S-Zn-β-TCP/SA/PEG increased with the extension of mineralization time. The thickest mineralized coating of Monetite/SA/PEG was higher than that of the SA/PEG, indicating Monetite could enhance the effect of mineralization. Notably, the tooth slices treated with S-Zn-β-TCP/SA/PEG exhibited the thickest mineralized coating, showing significant differences compared to SA/PEG and Monetite/SA/PEG, as shown in Fig. 11B.

From Figs. 10A and 11A, it could be observed that the addition of PEG-4000 to the paste not only accelerated the mineralization rate but also improved the mineralization-inducing effect of the paste on the tooth slices. The related studies have shown that PEG coatings could effectively improve the hydrophilicity and mineralization characteristics of calcium phosphate [81]. Furthermore, compared to the loose mineralized coating induced by S-Zn-β-TCP/SA, the mineralized layer induced by S-Zn-β-TCP/SA/PEG was dense and tightly adhered to the tooth slices, owing to the excellent viscosity and mineralization-inducing properties of PEG [82,83]. Siddaramaiah et al. demonstrated that the mixture of sodium alginate and PEG still maintained good viscosity [84]. These findings collectively suggested that S-Zn-β-TCP/SA/PEG rapidly induced the formation of dense and closely adhering mineralized coatings on the tooth slices, effectively sealing dentinal tubules and holding potential as a treatment for dentin hypersensitivity.

Herein, we prepared Monetite and Zn-β-TCP with different sizes by adding zinc and adjusting the amount of ammonia, and mixed them with sodium alginate and polyethylene glycol to prepare a paste for the treatment of dentin allergy. The Zn^{2+} played a dual role in regulating the structure and biological function of β-TCP, while the change of ammonia content regulated the size of Zn-β-TCP. Trace element-modified CaPs have been proven to be an effective material for repairing defective hard tissue [85]. The results of biological functions evaluation *in vitro* demonstrated that Zn-β-TCP had better effects on enhancing proliferation, dentin differentiation, and antibacterial than those of the control group and Monetite. Monetite S-Zn-β-TCP and B-Zn-β-TCP were mixed with SA respectively to construct a powerful delivery platform to deliver the target materials with induced mineralization, good biocompatibility, and excellent antibacterial effect to the lesion location. The induced mineralization and viscosity properties of SA have been widely recognized, and the addition of PEG-4000 was to further improve the viscosity and induced mineralization rate of the paste [22,25]. The *in vitro* viscosity test and tooth slice mineralization test showed that compared with S-Zn-β-TCP/SA, the viscosity of S-Zn-β-TCP/SA/PEG was higher, the formation efficiency of an induced mineralized layer was faster and the mineralized layer was denser. Taken together, S-Zn-β-TCP/SA/PEG paste provides a good method for dentin hypersensitivity and possesses great application potential in hard tissue engineering and regenerative medicine.

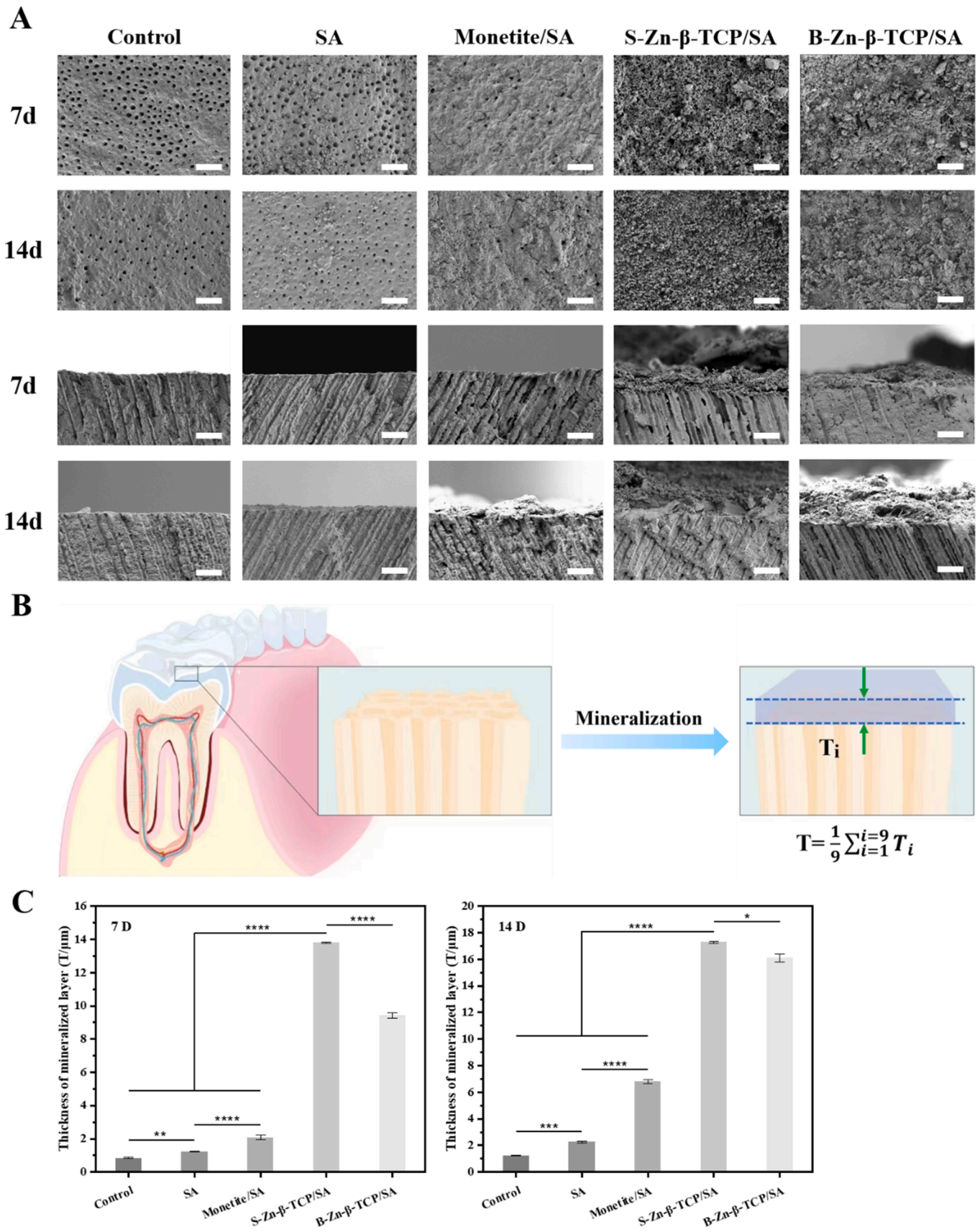

Fig. 10. The mineralization evaluation of pastes on tooth slices *in vitro*. (A) SEM images of top and cross-sectional surfaces of tooth slices treated with SA, Monetite/SA, S-Zn-β-TCP/SA, and B-Zn-β-TCP/SA in simulated saliva for 7 and 14 days; scale bar=20 μm. (B) Schematic diagram of thickness measurement of mineralized layer. (C) Quantitative analysis of the thickness of the mineralized layer. ($n = 3$, $^{***}P < 0.001$).

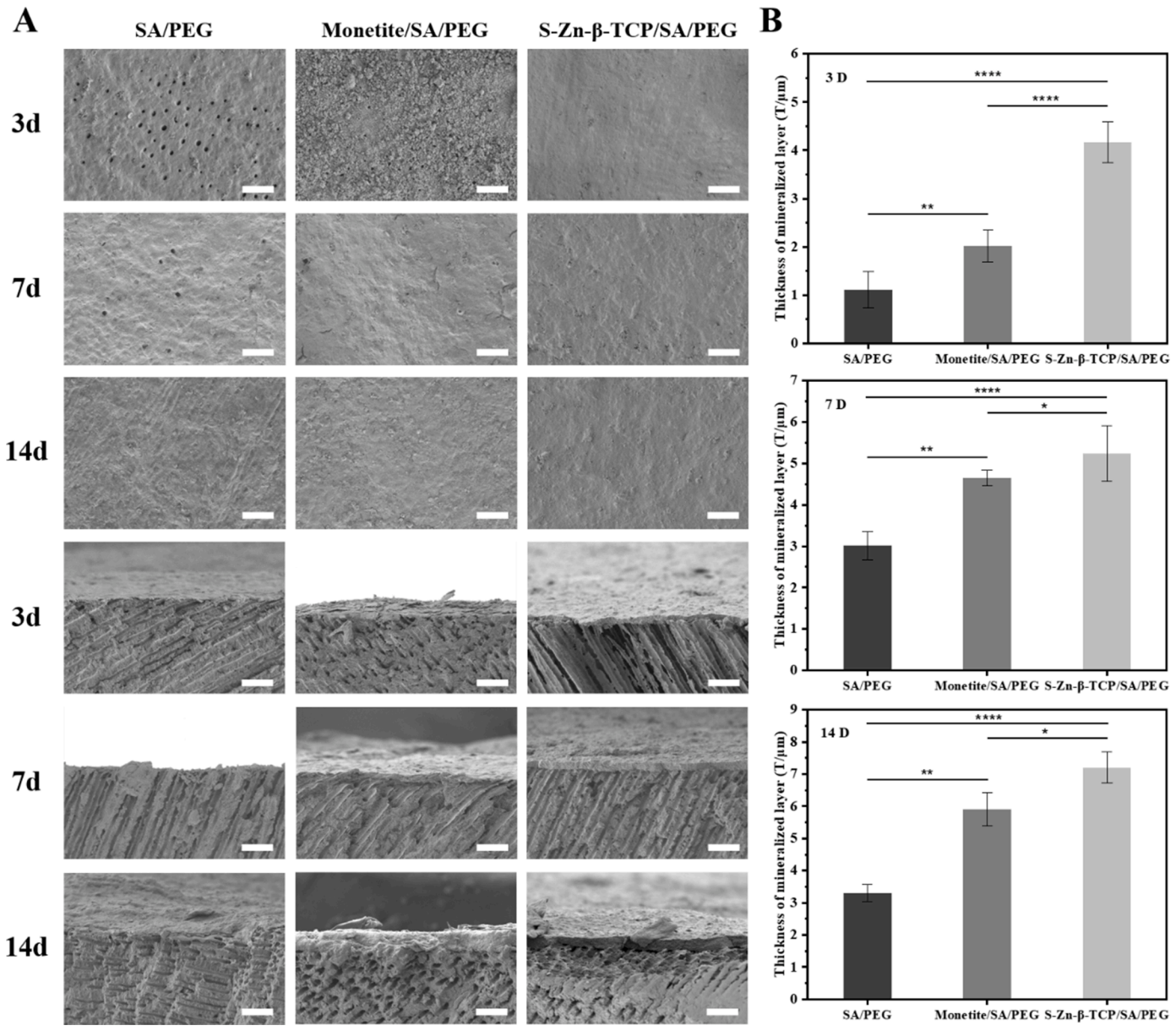

Fig. 11. The mineralization evaluation of tooth slices *in vitro*. (A) SEM images of top and cross-sectional surfaces of tooth slices treated with SA/PEG, Monetite/SA/PEG, S-Zn-β-TCP/SA/PEG in simulated saliva for 3, 7, and 14 days; scale bar=20 μm. (B) Quantitative analysis of the thickness of the mineralized layer. ($n = 3$, $^*P < 0.05$).

CaPs are the main inorganic component of human hard tissue, which has many advantages, such as good biocompatibility, good effect of induced mineralization, low preparation cost, and green environmental protection [86]. Zn^{2+} is one of the essential trace elements in the human body, which plays an important role in tissue growth and human metabolism, so it can be used to improve or make up for some specific biological functions of biomaterials [15]. SA and PEG not only have a good effect of inducing mineralization but also can be degraded under physiological conditions. In addition, PEG and SA belong to polycationic and polyanionic polymers respectively, which provide a theoretical basis for further improving the mineralization rate of S-Zn-β-TCP/SA/PEG [33]. However, the mineralized layer induced by S-Zn-β-TCP/SA/PEG was located on the surface of the tooth section and did not go deep into the dentinal tubule, and the mechanical collision on the tooth surface caused by daily diet and tooth brushing will cause the mineralized layer to fall off, thus losing the therapeutic effect. Furthermore, the viscosity test of the paste was limited to the erosion of water flow and did not simulate the mechanical effect of the real oral environment on the paste. To further improve the feasibility of S-β-TCP/SA/PEG paste in the clinical treatment of dentin hypersensitivity, future studies will focus on rapidly inducing the formation of mineralized layer in dentinal tubules and verifying the bonding strength of mineralized layer by brushing teeth and simulating mastication.

4. Conclusions

In conclusion, our study successfully synthesized Monetite, S-Zn-β-TCP, and B-Zn-β-TCP particles by hydrothermal method. The *in vitro* studies revealed that these particles possessed outstanding mineralization-inducing capabilities and biocompatibility. Furthermore, S-Zn-β-TCP and B-Zn-β-TCP demonstrated notable antibacterial effects and potential for promoting dentinogenesis. The paste prepared by combining Monetite, S-Zn-β-TCP, and B-Zn-β-TCP with sodium alginate, namely Monetite/SA, S-Zn-β-TCP/SA, and B-Zn-β-TCP/SA, could induce the formation of mineralized coatings on the surfaces of dentin slices, effectively sealing dentinal tubules. Among these pastes, the S-Zn-

β-TCP/SA exhibited the best sealing effect. The addition of PEG-4000 to the paste enhanced their viscosity and mineralization-inducing capabilities. The *in vitro* flushing and mineralization results indicated that SA/PEG, Monetite/SA/PEG, and S-Zn-β-TCP/SA/PEG induced faster mineralization on dentin slices compared to SA, Monetite/SA, and S-Zn-β-TCP/SA. Moreover, compared to S-Zn-β-TCP/SA, S-Zn-β-TCP/SA/PEG not only had higher mineralization efficiency and viscosity but also formed a denser mineralized coating that adhered more closely to the dentin slices. The S-Zn-β-TCP/SA/PEG paste possessed excellent viscosity, antibacterial, and mineralization-inducing properties developed in the current study and held great potential use for the treatment of dentin hypersensitivity.

CRediT authorship contribution statement

Hao Huang: Writing – review & editing, Writing – original draft, Methodology, Investigation, Conceptualization. **Minjie Fan:** Writing – review & editing, Data curation, Validation. **Anchun Yang:** Investigation, Formal analysis. **Dongbiao Chang:** Methodology, Data curation. **Jinsheng Li:** Writing – review & editing, Formal analysis, Data curation. **Liwen Yang:** Investigation, Methodology. **Xinlun Li:** Methodology, Investigation. **Mengyuan Wang:** Supervision, Formal analysis, Writing – review & editing, Conceptualization. **Pengfei Zheng:** Writing – review & editing, Supervision, Project administration, Funding acquisition. **Tailin Guo:** Writing – review & editing, Supervision, Funding acquisition. **Jie Weng:** Writing – review & editing, Supervision, Funding acquisition, Conceptualization.

Declaration of competing interest

The authors declare that they have no known competing financial interests or personal relationships that could have appeared to influence the work reported in this paper.

Data availability

No data was used for the research described in the article.

Acknowledgments

This work was supported by the National Natural Science Foundation of China (52071277, 32071343), China Postdoctoral Science Foundation (2022M721685); China Postdoctoral Science Foundation Special Grant Program (2023T160331); Fundamental Research Funds for Central University (2682020ZT80).

Supplementary materials

Supplementary material associated with this article can be found, in the online version, at doi:10.1016/j.apmt.2024.102171.

References

[1] A. Davari, E. Ataei, H.J. Assarzadeh, Dentin hypersensitivity: etiology, diagnosis and treatment; a literature review, J. Dent. 14 (2013) 136–145.
[2] Z. Ling, Y. He, H. Huang, X. Xie, Q.L. Li, C.Y. Cao, Effects of oligopeptide simulating DMP-1/mineral trioxide aggregate/agarose hydrogel biomimetic mineralisation model for the treatment of dentine hypersensitivity, J. Mater. Chem. B 7 (38) (2019) 5825–5833.
[3] N.X. West, M. Sanz, A. Lussi, D. Bartlett, P. Bouchard, Prevalence of dentine hypersensitivity and study of associated factors: a European population-based cross-sectional study, J. Orofac. Orthop. 41 (10) (2013) 841–851.
[4] X. Yu, L. Bing, X. Jin, B. Fu, M. Hannig, Comparative *in vivo* study on the desensitizing efficacy of dentin desensitizers and one-bottle self-etching adhesives, Oper. Dent. 35 (3) (2010) 279–286.
[5] M.S. Thomas, Dentin hypersensitivity, J. Evid. Based Dent. Pract. 142 (3) (2011) 220–228.
[6] M. Vano, G. Derchi, A. Ba Rone, U. Covani, Effectiveness of nano-hydroxyapatite toothpaste in reducing dentin hypersensitivity: a double-blind randomized controlled trial, Quintessence Int. 45 (8) (2014) 703–711.
[7] R.J. Palmer, S. Periasamy, N.S. Jakubovics, Oral multispecies biofilm development and the key role of cell-cell distance, Nat. Rev. Microbiol. 8 (7) (2010) 471–480.
[8] D.K.F. Jones, G.P. Andrews, D.S. Jones, Strontium-containing, carbohydrate-based polymer networks as tooth-adherent systems for the treatment of dentine hypersensitivity, Carbohydr. Polym. 157 (2017) 400–408.
[9] N. Baheiraei, M.R. Nourani, S.M.J. Mortazavi, M. Movahedin, H. Eyni, F. Bagheri, M.H. Norahan, Development of a bioactive porous collagen/beta-tricalcium phosphate bone graft assisting rapid vascularization for bone tissue engineering applications, J. Biomed. Mater. Res. A 106 (1) (2018) 73–85.
[10] D. Huang, B. He, P. Mi, Calcium phosphate nanocarriers for drug delivery to tumors: imaging, therapy and theranostics, Biomater. Sci. 7 (10) (2019) 3942–3960.
[11] M. Bohner, B.L.G. Santoni, N. Dobelin, β-tricalcium phosphate for bone substitution: synthesis and properties, Acta Biomater. 113 (2020) 23–41.
[12] K. Wang, Y. Leng, X. Lu, F. Ren, Calcium phosphate bioceramics induce mineralization modulated by proteins, Mater. Sci. Eng. C. 33 (6) (2013) 3245–3255.
[13] S. Shinichiroh, M. Keiichi, H. Takahiro, T. Yasuhiro, T. Toshihiko, A new β-tricalcium phosphate with uniform triple superporous structure as a filling material after curettage of bone tumor, Anticancer Res. 33 (11) (2013) 5075–5081.
[14] M.H. AlRefeai, E.M. AlHamdan, S. Al-Saleh, A.S. Alqahtani, M.Q. Al-Rifaiy, I. F. Alshiddi, I. Farooq, F. Vohra, T. Abduljabbar, Application of beta-tricalcium phosphate in adhesive dentin bonding, Polymers 13 (17) (2021) 2855–2866.
[15] Y. Su, I. Cockerill, Y. Wang, Y.X. Qin, L. Chang, Y. Zheng, D. Zhu, Zinc-based biomaterials for regeneration and therapy, Trends Biotechnol. 37 (4) (2019) 428–441.
[16] Y. Huang, Q. Gao, C. Li, X. Chen, X. Li, Y. He, Q. Jin, J. Ji, Facile synthesis of Zn2+-based hybrid nanoparticles as a new paradigm for the treatment of internal bacterial infections, Adv. Funct. Mater. 32 (15) (2021) 2109011.
[17] Y. Chen, J. Cai, D. Liu, S. Liu, D. Lei, L. Zheng, Q. Wei, M. Gao, Zinc-based metal organic framework with antibacterial and anti-inflammatory properties for promoting wound healing, Regen. Biomater. 9 (1) (2022) rbac019.
[18] Y.W. Wang, A. Cao, Y. Jiang, X. Zhang, H. Wang, Superior antibacterial activity of ZnO/graphene oxide composites originated from high zinc concentration localized around bacteria, ACS Appl. Mater. Interfaces 6 (4) (2014) 2791–2798.
[19] M. Ikeuchi, A. Ito, Y. Dohi, H. Ohgushi, H. Shimaoka, K. Yonemasu, T. Tateishi, Osteogenic differentiation of cultured rat and human bone marrow cells on the surface of zinc-releasing calcium phosphate ceramics, J. Biomed. Mater. Res. A 67 (4) (2003) 1115–1122.
[20] G. Meng, X. Wu, R. Yao, J. He, W. Yao, F. Wu, Effect of zinc substitution in hydroxyapatite coating on osteoblast and osteoclast differentiation under osteoblast/osteoclast co-culture, Regen. Biomater. 6 (6) (2019) 11.
[21] X. Zhang, D. Yao, W. Zhao, R. Zhang, B. Yu, G. Ma, Y. Li, D. Hao, F.J. Xu, Engineering platelet-rich plasma based dual-network hydrogel as a bioactive wound dressing with potential clinical translational value, Adv. Funct. Mater. 31 (8) (2020) 2009258.
[22] R.E. Abouzeid, R. Khiari, A. Salama, M. Diab, A. Dufresne, *In situ* mineralization of nano-hydroxyapatite on bifunctional cellulose nanofiber/polyvinyl alcohol/sodium alginate hydrogel using 3D printing, Int. J. Biol. Macromol. 160 (2020) 538–547.
[23] S.N. Pawar, K.J. Edgar, Alginate derivatization: a review of chemistry, properties and applications, Biomaterials 33 (11) (2012) 3279–3305.
[24] L. Liu, Y. Xiang, Z. Wang, X. Yang, X. Yu, Y. Lu, L. Deng, W.G. Cui, Adhesive liposomes loaded onto an injectable, self-healing and antibacterial hydrogel for promoting bone reconstruction, NPG Asia Mater. 81 (2019) 11:81.
[25] M. Gan, Q. Zhou, J. Ge, J. Zhao, Y.J. Wang, Q. Yan, C.H. Wu, H. Yu, Q. Xiao, W. X. Wang, H.L. Yang, J. Zou, Precise *in-situ* release of microRNA from an injectable hydrogel induces bone regeneration, Acta Biomater. 135 (2021) 289–303.
[26] Y. Ding, K. Zhai, P. Pei, Y. Lin, Y. Ma, H. Zhu, M. Shao, X. Yang, W. Tao, Encapsulation of cisplatin in a pegylated calcium phosphate nanoparticle (CPNP) for enhanced cytotoxicity to cancerous cells, J. Colloid Interface Sci. 493 (2017) 181–189.
[27] D. Igdem, W. Evita, Y. Chai, L. Frank, P. Jennifer, Cell-mediated mineralization of synthetic polyethylene glycol hydrogels to create bone tissue engineering constructs, Front. Bioeng. Biotechnol. 4 (2016) 1–2.
[28] D.K. Thomas, A. Charlesby, Viscosity relationship in solutions of polyethylene glycols, J. Polym. Sci. 42 (139) (1960) 195–202.
[29] J.S. Jang, S.Y. Kim, S.B. Lee, K.O. Kim, J.S. Han, Y.M. Lee, Poly(ethylene glycol)/poly(epsilon-caprolactone) diblock copolymeric nanoparticles for non-viral gene delivery: the role of charge group and molecular weight in particle formation, cytotoxicity and transfection, J. Control. Release 113 (2) (2006) 173–182.
[30] Q. Yu, Y. Tian, M. Li, Y. Jiang, J.W. Cui, Poly(ethylene glycol)-mediated mineralization of metal-organic frameworks, Chem. Commun. 56 (75) (2020) 11078–11081.
[31] L. Peng, L. Chang, X. Liu, J. Lin, H. Liu, B. Han, S. Wang, Antibacterial property of a polyethylene glycol-grafted dental material, ACS Appl. Mater. Interfaces 9 (21) (2017) 17688–17692.
[32] C. Li, D. Lu, J. Deng, X. Zhang, P. Yang, Amyloid-like rapid surface modification for antifouling and in-depth remineralization of dentine tubules to treat dental hypersensitivity, Adv. Mater. 31 (46) (2019) 1903973.
[33] K. Bhagyasree, D. Mukherjee, M. Azamthulla, S. Debnath, L.M. Sundar, S. Hulikal, B.V. Teja, S. Bhatt, D. Kamnoore, Thiolated sodium alginate/polyethylene glycol/

hydroxyapatite nanohybrid for bone tissue engineering, J. Drug Deliv. Sci. Technol. 76 (2022) 103813.
[34] P.D. Patil, V.R. Shaikh, G.R. Gupta, D.G. Hundiwale, A.U. Borse, K.J. Patil, Studies of Viscosity Coefficient and Expansivity Properties of Aqueous Solutions of Ethylene Glycol and Polyethylene Glycols at 293.15, 298.15 and 303.15K and at Ambient Pressure, J. Solut. Chem. 45 (6) (2016) 947–969.
[35] E.J.H. van Dijk, M. Pronk, M.C.M. van Loosdrecht, A settling model for full-scale aerobic granular sludge, Water Res. 186 (2020) 116135.
[36] S. Gomes, J.M. Nedelec, E. Jallot, D. Sheptyakov, G. Renaudin, Unexpected mechanism of Zn^{2+} insertion in calcium phosphate bioceramics, Chem. Mater. 23 (12) (2011) 3072–3085.
[37] A. Ito, M. Otsuka, H. Kawamura, M. Ikeuchi, H. Ohgushi, Y. Sogo, N. Ichinose, Zinc-containing tricalcium phosphate and related materials for promoting bone formation, Curr. Appl. Phys. 5 (5) (2005) 402–406.
[38] F. Miyaji, Y. Kono, Y. Suyama, Formation and structure of zinc-substituted calcium hydroxyapatite, Mater. Res. Bull. 40 (2) (2005) 209–220.
[39] Y. Sogo, A. Ito, K. Fukasawa, T. Sakurai, N. Ichinose, Zinc containing hydroxyapatite ceramics to promote osteoblastic cell activity, Mater. Sci. Technol. 20 (9) (2004) 1079–1083. Lond.
[40] B. Liu, X.M. Shi, G.Y. Xiao, Y.P. Lu, *In-situ* preparation of scholzite conversion coatings on titanium and Ti-6Al-4V for biomedical applications, Colloid Surf. B 153 (2017) 291–299. Complete.
[41] H. Alioui, O. Bouras, J.C. Bollinger, Toward an efficient antibacterial agent: Zn- and Mg-doped hydroxyapatite nanopowders, J. Environ. Sci. Health A 54 (3–4) (2019) 315–327.
[42] K. He, M. Sawczyk, C. Liu, Y.F. Yuan, B. Song, R. Deivanayagam, A. Nie, X. Hu, V. P. Dravid, J. Lu, C. Sukotjo, Y.P. Lu, P. Král, T. Shokuhfar, R. Shahbazian-Yassar, Revealing nanoscale mineralization pathways of hydroxyapatite using *in situ* liquid cell transmission electron microscopy, Sci. Adv. 6 (2020) eaaz7524.
[43] A. Dosen, R.F. Giese, Thermal decomposition of brushite, $CaHPO_4{\bullet}2H_2O$ to monetite $CaHPO_4$ and the formation of an amorphous phase, Am. Mineral. 96 (2/3) (2011) 368–373.
[44] D.W. Fan, S.Y. Wei, M.N. Ma, Z.Q. Chen, B.S. Li, H.S. Xie, High-pressure elastic behavior of $Ca_4La_6(SiO_4)_6(OH)_2$ a synthetic rare-earth silicate apatite: a powder X-ray diffraction study up to 9.33 GPa, Phys. Chem. Miner. 41 (2014) 85–90.
[45] G. Karunakaran, G.S. Kumar, E.B. Cho, Y. Sunwoo, E. Kolesnikov, D. Kuznetsov, Microwave-assisted hydrothermal synthesis of mesoporous carbonated hydroxyapatite with tunable nanoscale characteristics for biomedical applications, Ceram. Int. 45 (1) (2018) 970–977.
[46] E. Mhla, P.G. Koutsoukos, Heterogeneous crystallization of calcium hydrogen phosphate anhydrous (monetite), Colloid Surf. A 513 (2017) 125–135.
[47] M.M. Ferreira, A.F. Brito, D. Brazete, I.C. Pereira, E. Carrilho, A.M. Abrantes, A. S. Pires, M.J. Aguiar, L. Carvalho, M.F. Botelho, J.M.F. Ferreira, Doping β-TCP as a strategy for enhancing the regenerative potential of composite β-TCP-alkali-free bioactive glass bone grafts. experimental study in rats, Materials 12 (1) (2018) 4.
[48] L.P. Higuita, A.F. Vargas, M.J. Gil, L.F. Giraldo, Synthesis and characterization of nanocomposite based on hydroxyapatite and monetite, Mater. Lett. 175 (2016) 169–172.
[49] W. Wang, H. Tian, G. Shu, D. Huo, F. Zhang, X. Zhu, A bimetallic thermally regenerative ammonia-based battery for high power density and efficiently harvesting low-grade thermal energy, J. Mater. Chem. A 7 (2019) 5991–6000.
[50] W. Aware, T. Documentation, Implants for surgery-*In vitro* evaluation for apatite-forming ability of implant materials, Int. Sta. (2007) ISO23317.
[51] K. Shin, T. Acri, S. Geary, A.K. Salem, Biomimetic mineralization of biomaterials using simulated body fluids for bone tissue engineering and regenerative medicine, Tissue Eng. Part A 23 (19–20) (2017) 1169–1180.
[52] S. Tan, S. Chen, Q. Lei, D. Ma, A novel rapidly mineralized biphasic calcium phosphate with high acid-resistance stability for long-term treatment of dentin hypersensitivity, Dent. Mater. 39 (3) (2023) 260–274.
[53] R. Chakraborty, M. Monalisa, P. Saha, Electrochemical stability and bio-mineralization capability of zinc substituted and elemental zinc reinforced calcium phosphate composite coatings synthesized through pulsed electro-deposition, Ceram. Int. 45 (17) (2019) 22899–22911.
[54] L.L. Hench, J.M. Polak, Third-generation biomedical materials, Science 295 (5557) (2002) 1014–1017.
[55] G. Cama, S. Nkhwa, B. Gharibi, A. Lagazzo, R. Cabella, C. Carbone, P. Dubruel, H. Haugen, L.D. Silvio, S. Deb, The role of new zinc incorporated monetite cements on osteogenic differentiation of human mesenchymal stem cells, Biomater. Adv. 78 (2017) 485–494.
[56] M. Huang, R.G. Hill, S.C.F. Rawlinson, Zinc bioglasses regulate mineralization in human dental pulp stem cells, Dent. Mater. 33 (5) (2017) 543–552.
[57] A. Bakopoulou, E. Papachristou, M. Bousnaki, C. Hadjichristou, E. Kontonasaki, A. Theocharidou, L. Papadopoulou, N. Kantiranis, G. Zachariadis, G. Leyhausen, Human treated dentin matrices combined with Zn-doped, Mg-based bioceramic scaffolds and human dental pulp stem cells towards targeted dentin regeneration, Dent. Mater. 32 (8) (2016) e159–e175.
[58] C. Li, F. Sun, J. Tian, J. Li, H. Sun, Y. Zhang, S. Guo, Y. Lin, X. Sun, Y. Zhao, Continuously released Zn^{2+} in 3D-printed PLGA/beta-TCP/Zn scaffolds for bone defect repair by improving osteoinductive and anti-inflammatory properties, Bioact. Mater. 24 (2023) 361–375.
[59] N. Kawashima, Characterisation of dental pulp stem cells: a new horizon for tissue regeneration? Arch. Oral Biol. 57 (11) (2012) 1439–1458.
[60] S. Gronthos, J. Brahim, W. Li, L.W. Fisher, N. Cherman, A. Boyde, P. Denbesten, P. G. Robey, S. Shi, Stem cell properties of human dental pulp stem cells, J. Dent. 81 (8) (2002) 531.
[61] H. Sun, C. Wu, K. Dai, J. Chang, T. Tang, Proliferation and osteoblastic differentiation of human bone marrow-derived stromal cells on akermanite-bioactive ceramics, Biomaterials 27 (33) (2006) 5651–5657.
[62] H.S. Ching, N. Luddin, I.A. Rahman, K.T. Ponnuraj, Expression of odontogenic and osteogenic markers in DPSCs and SHED: a review, Curr. Stem Cell Res. Ther. 12 (1) (2017) 71–79.
[63] D. Tziafas, K. Kodonas, Differentiation potential of dental papilla, dental pulp, and apical papilla progenitor cells, J. Endod. 36 (5) (2010) 781–789.
[64] H. Mizumachi, S. Yoshida, A. Tomokiyo, D. Hasegawa, S. Hamano, A. Yuda, H. Sugii, S. Serita, H. Mitarai, Calcium-sensing receptor-ERK signaling promotes odontoblastic differentiation of human dental pulp cells, Bone 101 (2017) 191–201.
[65] C. Mi, Z. Jing, W. Zhu, A novel universal adhesive for improved dentin remineralization with antibiofilm potential against Streptococcus mutans and other cariogenic-pathogens, Int. J. Adhes. Adhes. 118 (2022) 103189.
[66] A. Vijayakumar, H.B. Sarveswari, S. Vasudevan, K. Shanmugam, A.P. Solomon, P. Neelakantan, Baicalein inhibits streptococcus mutans biofilms and dental caries-related virulence phenotypes, Antibiotics 10 (2) (2021) 215.
[67] Y. Ding, W. Wang, M. Fan, Z. Tong, R. Kuang, Antimicrobial and anti-biofilm effect of Bac8c on major bacteria associated with dental caries and Streptococcus mutans biofilms, Peptides 52 (2014) 61–67.
[68] C. Spengler, N. Thewes, F. Nolle, T. Faidt, N. Umanskaya, M. Hannig, M. Bischoff, K. Jacobs, Enhanced adhesion of Streptococcus mutans to hydroxyapatite after exposure to saliva, J. Mol. Recognit. 30 (7) (2017) e2615.
[69] D. Huang, Z. Luo, X. Zhou, Effect of calcium on adherence of streptococcus mutans MT6R (Serotype c) surface protein P1, West. China, J. Stomatol. 18 (3) (2000) 153.
[70] J. Xu, G. Ding, J. Li, S. Yang, B. Fang, H. Sun, Y. Zhou, Zinc-ion implanted and deposited titanium surfaces reduce adhesion of Streptococccus mutans, Appl. Surf. Sci. 256 (24) (2010) 7540–7544.
[71] Y. Liu, T. Kohno, R. Tsuboi, H. Kitagawa, S. Imazato, Acidity-induced release of zinc ion from BioUnionTMfiller and its inhibitory effects against Streptococcus mutans, Dent. Mater. J. 39 (4) (2020) 547–553.
[72] L.R. de Lacerda, M. Mitterhofer, W.J. Carvalho, F. GalbiattiCarlo, H. LemesPiva, E. A. Munchow, New generation bulk-fill resin composites: effects on mechanical strength and fracture reliability, J. Mech. Behav. Biomed. Mater. 96 (2019) 214–218.
[73] Y.P.G. Jimenez, H.R. Morales, J.W. Hernandez-Luis, Measurement and modelling of water activity, density and viscosity of the $KClO_4$ + poly(ethylene glycol) + H_2O system at various temperatures, J. Mol. Liq. 286 (2019) 110922.
[74] A.H.P. Chan, I. Jain, B.P. Oropeza, T. Zhou, B. Nelsen, N.A. Geisse, N.F. Huang, Combinatorial extracellular matrix cues with mechanical strain induce differential effects on myogenesis *in vitro*, Biomater. Sci. 11 (2023) 5893–5907.
[75] J.W. Wu, M.J. Liu, L. Wang, G.P. Guan, Influence of silk fibroin/sodium alginate coatings on the mineralization of silk fibroin fiber artificial ligament prototypes, Text. Res. J. 90 (13–14) (2020) 1590–1601.
[76] E. Kalantari, S.M. Naghib, M.R. Naimi-Jamal, A. Aliahmadi, M. Mozafari, Nanostructured monticellite for tissue engineering applications-Part I: microstructural and physicochemical characteristics, Ceram. Int. 44 (11) (2018) 12731–12738.
[77] L. Iskandar, L. Rojo, L.D. Silvio, S. Deb, The effect of chelation of sodium alginate with osteogenic ions, calcium, zinc, and strontium, J. Biomater. Appl. 34 (4) (2019) 1904.
[78] J. Guo, X. Shu, H. Deng, J. Zhang, Y. Wang, G. Meng, J. He, F. Wu, Stiff and tough hydrogels prepared through integration of ionic cross-linking and enzymatic mineralization, Acta Biomater. 149 (2022) 220–232.
[79] Q. Huang, Z. Liang, J. Li, Z. Lin, Size dependence of particulate calcium phosphate fillers in dental resin composites, ACS Omega 6 (50) (2021) 35057–35066.
[80] H. Xu, G. Zhang, K. Xu, L. Wang, X. Qiu, Mussel-inspired dual-functional PEG hydrogel inducing mineralization and inhibiting infection in maxillary bone reconstruction, Biomater. Adv. 90 (2018) 379–386.
[81] K. Liu, J. Sun, Q. Zhu, X. Jin, Z. Zhang, Z. Zhao, G. Chen, C. Wang, H. Jiang, P. Zhang, Microstructures and properties of polycaprolactone/tricalcium phosphate scaffolds containing polyethylene glycol fabricated by 3D printing, Ceram. Int. 48 (16) (2022) 24032–24043.
[82] N.J. Hempel, T. Dao, M.M. Knopp, R. Berthelsen, K. Lbmann, The influence of temperature and viscosity of polyethylene glycol on the rate of microwave-induced *in situ* amorphization of celecoxib, Molecules 26 (1) (2020) 110.
[83] A.P. Tiwari, M.K. Joshi, J. Lee, B. Maharjan, S.W. Ko, C.H. Park, C.S. Kim, Heterogeneous electrospun polycaprolactone/polyethylene glycol membranes with improved wettability, biocompatibility, and mineralization, Colloid Surf. A 520 (2017) 105–113.
[84] Siddaramaiah, T.M. Swamy, Studies on miscibility of sodium alginate/polyethylene glycol blends, J. Macromol. Sci. A 44 (3) (2007) 321–327.
[85] C. Xu, Y. Sun, J. Jansen, M. Li, L. Wei, Y. Wu, Y. Liu, Calcium phosphate ceramics and synergistic bioactive agents for osteogenesis in implant dentistry, Tissue Eng. Part C Methods 29 (5) (2023) 197–215.
[86] W. Habraken, P. Habibovic, M. Epple, M. Bohner, Calcium phosphates in biomedical applications: materials for the future? Mater. Today 19 (2) (2016) 69–87.